Main manuscript

Redefining the role of the *Plasmodium* heme detoxification protein: From hemozoin formation to mitochondrial protein synthesis

Louis Sarrazin[1], Joachim Kloehn[2], Tanja Ziesmann[3], Yasmin Schmitz[1], Anna-Lena Sandtmann[1], Robert Domènech-Eres[1], Katharina Scholz-Höhn[4], Coralie Boulet[2], Ute Distler[3,5], Joachim Michael Matz[1,*]

[1] Molecular Parasitology Group, Department of Cellular Parasitology, Bernhard Nocht Institute for Tropical Medicine, 20359 Hamburg, Germany

[2] Department of Microbiology and Molecular Medicine, Faculty of Medicine, University of Geneva, 1206 Geneva, Switzerland

[3] Institute for Immunology, University Medical Center Mainz, 55131 Mainz, Germany

[4] Electron Microscopy Unit, Bernhard Nocht Institute for Tropical Medicine, 20359 Hamburg, Germany

[5] Research Centre for Immunotherapy (FZI), University Medical Center Mainz, 55131 Mainz, Germany

* Correspondence: JMM, joachim.matz@bnitm.de

ORCIDs:

Louis Sarrazin	0000-0001-8404-338X
Joachim Kloehn	0000-0002-6366-8599
Tanja Ziesmann	0009-0009-0399-258X
Yasmin Schmitz	0009-0003-8683-1509
Anna-Lena Sandtmann	0009-0003-5979-3658
Robert Domènech-Eres	0009-0000-4779-2576
Katharina Scholz-Höhn	0009-0000-7008-0884
Coralie Boulet	0000-0002-5476-7800
Ute Distler	0000-0002-8031-6384
Joachim Michael Matz	0000-0002-0575-0412

ABSTRACT

Throughout their intraerythrocytic development, malaria parasites digest up to 80% of the host cell's hemoglobin within a specialized degradative compartment known as the digestive vacuole. This process releases heme, which is detoxified by sequestration into bioinert hemozoin crystals. Although heme biomineralization is essential for blood-stage survival and a validated drug target, its underlying mechanisms remain unclear. Initially identified as a potent inducer of β-hematin crystallization *in vitro*, the parasite's Heme Detoxification Protein (HDP) has been proposed to execute a similar role in the formation of hemozoin crystals *in cellulo*. Here, we investigate the function of HDP in live *Plasmodium falciparum* parasites, integrating experimental genetic approaches with quantitative microscopy, cellular bioenergetics and whole-proteome profiling. Endogenous tagging revealed that HDP localizes to the mitochondrion rather than the digestive vacuole. Conditional inactivation of HDP resulted in a gradual loss of mitochondrial membrane potential, preceding developmental arrest. Bypassing the essential role of the respiratory chain in pyrimidine biosynthesis – either through exogenous electron acceptors or expression of a ubiquinone-independent dihydroorotate dehydrogenase – rescued HDP-deficient parasites, indicating a role in maintaining respiratory chain activity. Consistent with this, electron flow through complex IV was abolished in rescued HDP-null parasites, increasing sensitivity to proguanil, an antimalarial that synergizes with respiratory chain inhibitors. We found that loss of HDP leads to a marked reduction of complexes III and IV, whose integrity depends on mitochondrial protein biosynthesis. Integration of quantitative proteomic data with structure-guided homology modelling supports a role for HDP as part of the large mitoribosomal subunit at the inter-subunit contact site. By contrast, neither the quantity nor morphology of hemozoin was affected by the loss of HDP, and sensitivity to the hemozoin-targeting drug chloroquine remained unchanged. Together, these findings challenge previous models linking HDP to hemozoin formation and instead reveal an essential role for HDP in mitochondrial protein biosynthesis.

KEY WORDS

malaria / *Plasmodium* / HDP / heme / hemozoin / mitochondrion / ribosome / electron transport chain

INTRODUCTION

Heme is a ubiquitous and evolutionarily ancient prosthetic group that plays a central role in a wide range of biological processes. It consists of a porphyrin ring coordinating a central iron atom (1), which can alternate between ferrous (Fe^{2+}) and ferric (Fe^{3+}) states, allowing it to accept and donate electrons in redox reactions and to bind small gaseous molecules reversibly. Heme-containing proteins include cytochromes, which facilitate electron transfer during photosynthesis and respiration, and globins, which bind gases for transport, storage, and sensing (2, 3). In addition, various enzymes use heme iron as a catalytic center to carry out diverse redox or radical reactions (4).

The limited bioavailability of iron and the high metabolic cost of heme biosynthesis can constrain growth and development. In pathogens, this constraint is amplified during infection, when hosts sequester heme and iron through nutritional immunity, which in turn drives the evolution of specialized acquisition strategies such as high affinity transport systems, siderophore based uptake pathways, and other mechanisms that enable pathogens to compensate for host imposed nutrient limitation (5). In this regard, malaria parasites differ markedly from most pathogens. These vector-borne protozoans replicate within red blood cells (RBCs), an environment exceptionally rich in heme (6). Although the parasite genome encodes a heme biosynthetic pathway, it is dispensable during blood-stage development and only becomes essential later in the mosquito vector and the human liver, where heme is less abundant (7-9).

Asexual blood-stage parasites nevertheless rely on heme-mediated reactions, particularly in the mitochondrial electron transport chain (ETC) (10). Their ETC is highly unusual among eukaryotes, as it is not required for ATP synthesis. Components of the ATP synthase (complex V) and enzymes of the tricarboxylic acid (TCA) cycle are dispensable at this stage, with most ATP generated via glycolysis (11-16). Nonetheless, the mitochondrion maintains an active ETC, in which electrons are sequentially passed along heme-containing cytochromes before ultimately reducing oxygen (17). This electron flow powers proton pumping by respiratory complexes III and IV, thereby generating a chemiosmotic gradient that helps sustain the mitochondrial membrane potential ($\Delta\Psi_{mt}$) (18).

The integrity of complexes III and IV depends on both cytosolic and mitochondrial protein synthesis. While most subunits are nuclear encoded and imported into the mitochondrion post-translationally, three proteins are encoded in the mitochondrial genome: cytochrome b of complex III, and cytochrome c oxidase subunits 1 (Cox1) and 3 (Cox3) of complex IV (19, 20). In apicomplexan parasites, these are the only proteins synthesized by the mitochondrial ribosome (mitoribosome). The mitoribosome is a large complex composed of highly fragmented rRNAs and both conserved as well as parasite-specific proteins, all organized into a large (LSU) and a small subunit (SSU), functionally streamlined to produce only these three proteins (21, 22).

Complex III receives electrons from the lipid-soluble carrier ubiquinol, a transfer that is essential for parasite survival, as illustrated by the antimalarial drug atovaquone, which blocks this reaction (23, 24). In most systems, ubiquinol is generated by dehydrogenases of the TCA cycle and by complex I which uses NADH to reduce ubiquinone. However, complex I is absent in malaria parasites. They instead possess an alternative single-subunit NADH:ubiquinone oxidoreductase, which is not required for blood-stage growth, similar to the dehydrogenases of the TCA cycle (11, 25, 26). This suggests that their contribution to feeding electrons into complex III is minor. The main enzyme donating electrons to complex III is believed to be dihydroorotate dehydrogenase (DHODH), which produces the pyrimidine precursor orotate and transfers the electrons to ubiquinone (10). Interestingly, the only essential role of complexes III and IV during asexual blood-stage development is to enable pyrimidine biosynthesis by serving as an electron sink that regenerates ubiquinone for DHODH activity (10). Bypassing this requirement, either by supplying alternative electron acceptors or by expressing a ubiquinone-independent DHODH, fully restores parasite viability when the terminal respiratory complexes are pharmacologically or genetically disrupted (10, 27).

The heme that enables electron transfer within the ETC is salvaged from the host RBC, whose protein content is >95% hemoglobin (7-9). Hemoglobin is endocytosed and transported to a lysosome-like organelle known as the digestive vacuole (DV), where it is proteolytically degraded, providing the parasite with amino acids and releasing heme for potential use (28). However, far more heme is mobilized than needed. Owing to its reactive nature, free heme iron is highly cytotoxic, damaging lipids, proteins and DNA (29, 30). Consequently, the parasite must balance its metabolic requirement for heme with an effective detoxification strategy. This is achieved by sequestering the vast majority of heme within the DV as bioinert hemozoin crystals (30, 31). Upon release from the globin chains, heme is first oxidized to hematin, which forms dimers through reciprocal iron-carboxylate bonds. These dimers then polymerize via hydrogen bonding to form the hemozoin crystals (32). Heme biomineralization is essential for parasite survival and is targeted by potent antimalarials, such as chloroquine, which inhibit adsorption of hematin onto the growing crystal surface (33-36).

The mechanism by which heme forms hemozoin remains debated. Minimalistic *in vitro* assays have been used to test how various additives affect the formation of β-hematin, a synthetic but structurally identical form of hemozoin. These studies have produced conflicting results, implicating lipids (37, 38), membranes (39), phase boundaries (40), and proteins (41, 42) as potential drivers of heme biomineralization. A few parasite proteins have been shown to modulate heme crystallization *in vitro*, and one even *in cellulo,* yet none appear essential for parasite survival (41, 43). The notable exception is the heme detoxification protein (HDP, PF3D7_1446800), which efficiently induces β-hematin formation *in vitro* and for which genetic evidence supports a critical role in parasite viability (14, 15, 42). Biochemical and imaging-based studies also indicate that HDP may reside in the DV, supporting a potential function in heme biomineralization (42, 44, 45). However, parasite-centered research approaches have yet to demonstrate this role *in cellulo*.

Here, we characterize the function of HDP in the human malaria pathogen *Plasmodium falciparum* using reverse genetic approaches. We show that HDP is not required for hemozoin formation, but participates in mitochondrial protein biosynthesis, likely as a component of the mitoribosome, which is essential for the integrity and function of the ETC. These findings represent a paradigm shift in the study of heme biomineralization, revealing an alternative role for a protein long considered the primary driver of hemozoin formation.

128 **RESULTS**

129 **HDP localizes to the parasite mitochondrion**

130 Previous studies have reported conflicting localizations for HDP, placing the protein in the RBC
131 cytosol, the DV, and elongated organelles within the parasite (42, 45). To clarify its precise subcellular
132 distribution, we endogenously fused mNeonGreen (mNG) to the C-terminus of HDP, allowing direct
133 visualization in live parasites. Simultaneously, we introduced two *loxP* sites into the HDP locus, one
134 within a synthetic intron near the start codon and another just downstream of the stop codon, facilitating
135 conditional reverse genetic experiments using the DiCre system (46) (Figure 1A, Supplementary Table
136 S1). Following transfection of the modifying construct into DiCre-expressing B11 parasites, two *hdp-*
137 *mNG:loxP* clones were isolated, and correct genomic integration was confirmed by diagnostic PCR
138 (Figure 1B).

139 Live fluorescence microscopy revealed mNG signal in a tubular parasite organelle, which
140 expanded dramatically during parasite maturation, and eventually branched and divided during
141 merozoite segmentation (Figure 1C). In addition, a faint green signal colocalized with the porphyrin-
142 derived red autofluorescence of the DV, but comparison with parental B11 parasites revealed that it did
143 not exceed the DV's baseline fluorescence (Figure 1C,D). To further examine a potential DV localization,
144 we overexpressed HDP fused to mCherry (mCh), but despite the much stronger fluorescence,
145 localization remained restricted to the branching organelle, with no apparent signal in the DV (Figure
146 1E).

147 The branching morphology of the HDP-containing compartment was reminiscent of the
148 parasite's two endosymbiotic organelles: the apicoplast and the mitochondrion. Thus, to determine the
149 precise localization of HDP, we further modified the *hdp-mNG:loxP* parasites to episomally express
150 minimal mCh-based reporters for both these organelles. No overlap was observed with the apicoplast
151 marker, whereas HDP exhibited near-complete colocalization with the mitochondrial reporter (Figure
152 1F). HDP also coincided with the $\Delta\Psi_{mt}$-dependent dye MitoTracker Red CMXRos (Figure 1F). Together,
153 these results suggest that HDP is absent from the DV and instead localizes to the parasite mitochondrion
154 throughout asexual blood stage development.

155 **HDP is critical for blood-stage survival**

156 To assess the importance of HDP for the parasite's blood-stage development, we induced its
157 excision from the genome by treating *hdp-mNG:loxP* cultures with 20 nM rapamycin (RAP) immediately
158 after invasion, thereby triggering DiCre-mediated recombination. Diagnostic PCRs of the HDP locus
159 confirmed RAP-induced loss of the target DNA compared to dimethyl sulfoxide (DMSO)-treated control
160 parasites (Figure 2A). Loss of the mNG-tagged protein was verified by Western blot analysis. In DMSO-
161 treated samples, mNG was detected in the detergent-resistant pellet fraction after parasite lysis,
162 appearing as a band of ~50 kDa, consistent with the expected size of the HDP-mNG fusion protein (52
163 kDa) (Figure 2B). An additional, more prominent band at ~80 kDa was also observed, indicative of
164 abnormal migration behavior during SDS-PAGE. Both bands were markedly depleted in lysates from
165 RAP-treated parasites by the end of the first intraerythrocytic cycle, coinciding with the disappearance
166 of mNG fluorescence in live microscopy, together confirming that HDP is efficiently removed upon RAP
167 treatment (Figure 2B,C).

168 We next monitored parasite morphology in tightly synchronized cultures by light microscopy of
169 Giemsa-stained blood smears over two intraerythrocytic cycles. While DMSO control parasites
170 developed normally, RAP treated parasites completed the first cycle but arrested development in the
171 second cycle as trophozoites (Figure 2D). Flow cytometry-assisted growth assays corroborated these
172 observations, showing that RAP-treated parasites underwent one successful round of replication but
173 failed to proliferate thereafter (Figure 2E,F). In contrast, the parental B11 line was unaffected by RAP
174 treatment (Figure 2G). Combined, these findings indicate that HDP is essential for the survival of *P.*
175 *falciparum* blood-stage parasites.

176 **Loss of hemozoin formation coincides with developmental arrest in HDP-null parasites**

To more precisely determine when developmental arrest occurs following HDP knockout, we treated ring-stage cultures with DMSO or RAP, allowed them to develop into mature schizonts, and used these schizonts to initiate a new, highly synchronous invasion. Samples were then collected every two hours, and parasite size was quantified microscopically in methanol-fixed blood smears. RAP-treated parasites ceased normal growth at approximately 21 hours post-invasion in the second cycle (Figure 2H).

We analyzed the same parasite populations using polarization microscopy, which specifically visualizes birefringent hemozoin crystals and thereby provides a quantitative measure of hemozoin content. In DMSO-treated control parasites, hemozoin levels steadily increased over time, whereas RAP-treated parasites began producing less hemozoin at around 20 hours post-invasion, coinciding with the onset of developmental arrest (Figure 2I). At 27 hours post-invasion, RAP-treated parasites contained 60% of the hemozoin found in controls. With parasite size also reduced to 59%, HDP-deficient parasites maintained comparable hemozoin content relative to size, and the crystals remained normally distributed, accumulating in a single large DV (Figure 2H,I). The fact that a similar reduction in hemozoin content was well tolerated in an unrelated mutant but coincides with death in HDP-deficient parasites further suggests that HDP has an essential function independent of heme biomineralization (43).

HDP is critical for maintaining the mitochondrial membrane potential

In light of these findings, we hypothesized that loss of HDP would primarily affect mitochondrial physiology. To test this, we assessed $\Delta\Psi_{mt}$ in DMSO and RAP-treated *hdp-mNG:loxP* parasites using MitoTracker Red CMXRos, which accumulates in mitochondria in a $\Delta\Psi_{mt}$-dependent manner. As a positive control, stained parasites were treated with carbonyl cyanide-p-trifluoromethoxyphenylhydrazone (FCCP), an ionophore that collapses $\Delta\Psi_{mt}$.

At 24 and 44 hours post-invasion in the first cycle, MitoTracker staining intensity was similar between DMSO- and RAP-treated parasites, while FCCP efficiently collapsed $\Delta\Psi_{mt}$ under both conditions (Figure 3A). In the second cycle, at 12 hours post-invasion, RAP-treated parasites already displayed a slight, non-significant reduction in MitoTracker intensity. This reduction became more pronounced and statistically significant at 18 hours post-invasion and persisted at later time points, showing an approximately two-fold decrease relative to DMSO-treated parasites (Figure 3A,B). Importantly, the dissipation of $\Delta\Psi_{mt}$ preceded the observed deficiencies in parasite size and hemozoin production (Figure 2H,I), indicating that mitochondrial depolarization upon loss of HDP is not a secondary consequence of parasite death.

A metabolic respiratory chain bypass rescues HDP-deficient parasites

Our findings led us to hypothesize that HDP may play a role in the ETC, the main contributor to $\Delta\Psi_{mt}$ (Figure 3C). Since the lethal effect of inhibiting mitochondrial respiration can be bypassed by alternative means of supporting dihydroorotate oxidation (10, 27), we tested whether exogenous supply of the electron acceptor decyl-ubiquinone (dQ) could rescue HDP-deficient parasites. Using standardized flow cytometry-assisted growth assays, we found that dQ enabled HDP-deficient parasites to replicate beyond the second cycle, indicating that restoration of DHODH activity was sufficient to compensate for the loss of HDP function (Figure 3D).

To further substantiate this, we tested whether expression of a ubiquinone-independent yeast DHODH could similarly rescue HDP-null parasites. We thus analyzed replication of the *hdp-mNG:loxP + mito-mCh + ydhodh* mutant that was used for mitochondrial colocalization. This line expresses yeast dihydroorotate dehydrogenase (yDHODH) as a drug-selectable marker, and we indeed found that it replicates efficiently even in the absence of HDP (Figure 3E). In contrast, *hdp-mNG:loxP + apico-mCh + bsd* parasites which express an unrelated blasticidin resistance cassette, still died in the second cycle after RAP treatment (Figure 3F). Together, these findings demonstrate that the loss of HDP can be largely compensated by bypassing the essential metabolic functions of the ETC.

Severely reduced respiration upon loss of HDP

These phenotypic rescue experiments suggested a role for HDP in mitochondrial respiration. To explore this further, we tested whether HDP influences sensitivity to proguanil, an antimalarial known to synergize with ETC inhibitors and thought to target a complex III/IV-independent pathway that supports mitochondrial polarization (10). Using replication-based drug susceptibility profiling of the rescued *hdp-mNG:loxP* + *mito-mCh* + *ydhodh* line, we found that loss of HDP increased parasite sensitivity to proguanil by approximately four-fold (Figure 3G). This indicates that loss of HDP sensitizes the parasites to respiration-independent mitochondrial depolarization, as expected in case of impaired electron transport.

To directly assess respiratory function, we measured oxygen consumption in DMSO- and RAP-treated second-cycle *hdp-mNG:loxP* + *mito-mCh* + *ydhodh* parasites at young schizont stage, using an XFe96 flux analyzer. RAP-treated parasites displayed a markedly reduced oxygen consumption rate (OCR) compared to DMSO controls under basal conditions (Figure 3H,I). Addition of the complex III inhibitor atovaquone to DMSO-treated parasites lowered the OCR to the same basal level observed in RAP-treated samples, while having little additional effect on the RAP-treated parasites themselves, together indicating a near-complete block of respiration in the absence of HDP. Addition of N,N,N′,N′-tetramethyl-p-phenylenediamine dihydrochloride (TMPD), which bypasses complex III by donating electrons directly to cytochrome c, restored oxygen consumption in DMSO-treated parasites, raising it far above basal levels, but failed to do so in RAP-treated samples (Figure 3H,I). This suggests that the respiratory defect in HDP-deficient parasites arises, at least in part, from dysfunction downstream of complex III.

Suspecting that complex IV dysfunction might underlie the respiratory defect, we endogenously tagged the subunits NDUFA4 and Cox5B with mCh in a yDHODH-rescued *hdp-mNG:loxP* background. Western blotting revealed a substantial reduction of both subunits in HDP-deficient parasites already by the end of the first cycle, indicating widespread disorganization and loss of complex IV in the absence of HDP (Figure 3J).

HDP is composed primarily of an adhesive protein domain

To better understand the role of HDP in the integrity and function of the ETC, we examined its molecular and structural features. HDP is predicted to consist primarily of a Fasciclin 1 (Fas1) domain, a widely conserved motif commonly involved in cell adhesion and, more rarely, in providing structural support within large protein assemblies (47, 48). Sequence alignment of HDP with representative Fas1-domain-containing proteins across diverse taxa revealed several conserved residues, including the histidine of the YH motif and residues within the H1 and H2 regions (47) (Figure 4A).

Structural prediction of HDP using AlphaFold 3 (49) produced a high-confidence model for the Fas1 domain, which aligned closely with the experimentally determined structure of a human Fas1 domain (50) (Figure 4B). In addition, HDP possesses a 48-residue N-terminal domain (NTD) enriched in positively charged and hydrophobic residues, consistent with a mitochondrial targeting signal. The NTD was modeled with low confidence and lacked a well-defined fold (Figure 4B). When fused to mCh, these 48 residues directed the reporter to the mitochondrion, supporting a role for the HDP N-terminus in mitochondrial targeting (Figure 4C).

HDP is the only protein encoded in the *P. falciparum* genome predicted to contain a Fas1 domain. In contrast, the related coccidian parasite *Toxoplasma gondii* encodes four such proteins: one of comparable size and overall architecture, TGME49_306050, and three significantly larger proteins (Figure 4D). Among the latter, TGME49_285272 was recently identified as a component of the mitoribosome large subunit (LSU) (21, 22). However, it contains an NTD more than eight times longer than that of HDP, and its Fas1 domain includes two extended loops absent from the *Plasmodium* protein (Figure 4D, Supplementary Figure S1). Despite these differences in overall architecture, the Fas1 domain of TGME49_285272 exhibited the highest sequence similarity to that of HDP among all *T. gondii* Fas1 proteins (Figure 4E). The AlphaFold model of TGME49_285272 Fas1 also showed the greatest

structural overlap with that of HDP, whereas the remaining *T. gondii* proteins aligned less closely – though this may partly reflect differences in model confidence (Figure 4E, Supplementary Figure S1). Finally, comparison with the experimentally determined structure of the TGME49_285272 Fas1 domain yielded the closest match to HDP, with only the human Fas1 domain achieving slightly better alignment (Figure 4E, Supplementary Figure S1).

HDP participates in mitochondrial protein biosynthesis

With the mitoribosomal protein TGME49_285272 identified as the most likely HDP ortholog, we predicted that loss of HDP would severely impair mitochondrial protein biosynthesis, the process responsible for producing the complex III component cytochrome b and the complex IV components Cox1 and Cox3 (19, 20). Consequently, HDP loss would be expected to destabilize not only complex IV, as reflected by reduced NDUFA4 and Cox5B (Figure 3J), but also complex III. To test this, we performed whole-cell proteome analysis of DMSO- versus RAP-treated *hdp-mNG:loxP + ydhodh* parasites. Nearly all subunits of complexes III and IV were markedly reduced upon HDP inactivation, with Cox1 and the complex IV component C4AP5 being completely undetectable in RAP-treated parasites (Figure 4F, Supplementary Table S2). In contrast, complex V, whose components are nuclear-encoded and imported into the mitochondrion post-translationally, remained unaffected, supporting a specific role of HDP in mitochondrial protein synthesis.

Among the proteins significantly reduced in HDP-deficient parasites were also multiple mitoribosomal components. Indeed, most mitoribosomal proteins showed lower abundance, though not all reached statistical significance (Figure 4G, Supplementary Table S2). This was generally more pronounced in the LSU than the SSU, with the LSU protein mRPL2 (PF3D7_1132700) being most affected (Figure 4H). Mapping these proteins onto the recently determined structure of the *T. gondii* mitoribosome revealed that the ortholog of mRPL2 is in direct contact with TGME49_285272, the protein we identified as the most likely HDP ortholog (Figure 4I). Both proteins localize to the LSU–SSU interface, potentially explaining why loss of HDP affects both subunits (Figure 4I,J). Destabilization was widespread across the LSU and SSU, indicating broad mitoribosomal instability upon HDP inactivation (Figure 4I,J; Supplementary Figure S2).

Collectively, these results suggest that HDP is an integral component of the LSU and critical for mitochondrial protein biosynthesis, which produces essential components for the stability and function of the malaria parasite's ETC.

HDP does not function in heme biomineralization

Finally, we revisited the previously proposed role of HDP in heme biomineralization by analyzing the quantity and morphology of hemozoin in metabolically rescued *hdp-mNG:loxP + mito-mCh + ydhodh* parasites. This approach allowed us to re-examine the pathway without confounding effects from developmental retardation. Parasites were analyzed 36 hours post-invasion in the second cycle, a time point at which HDP had been depleted for some time (Figure 2B,C), and well beyond when parasites lacking yDHODH would have died (Figure 2D,H). Using quantitative polarization microscopy, we observed no differences in the localization or amount of hemozoin between DMSO- and RAP-treated parasites (Figure 5A-C). Hemozoin crystals isolated from these parasites were examined by scanning electron microscopy, which revealed no HDP-dependent alterations in either size or morphology, with the crystals maintaining their characteristic brick-like elongated shape (Figure 5D). Finally, testing parasite sensitivity to chloroquine, a heme biomineralization inhibitor, showed no difference in the presence or absence of HDP (Figure 5E).

Together, our findings indicate that, despite previous reports of HDP-catalyzed β-hematin formation *in vitro*, HDP does not participate in hemozoin production in the parasite. Instead, our in-depth analysis of mitochondrial physiology places the protein in the mitoribosome.

DISCUSSION

Since Robert Virchow and Charles Laveran first recognized the connection between hemozoin and malaria (51, 52), generations of parasitologists have sought to understand how *Plasmodium* parasites orchestrate the formation of such highly ordered crystalline structures – a process that later turned out to be the target of several highly effective antimalarials (33, 35, 36). Early clues that parasite proteins might contribute to hemozoin formation came from observations that parasite lysates could catalyze β-hematin formation *in vitro* (53). In the search for specific parasite proteins capable of mediating this process, the first candidates examined were HRPII and III (41). Both proteins are present in the DV and contain repetitive histidine-rich stretches resembling heme-binding motifs. Although both proteins can efficiently catalyze β-hematin formation *in vitro*, they are dispensable for parasite survival, and their absence does not affect hemozoin production *in cellulo* (41). Recent evidence indicates that HRPII instead assembles into heme-rich nanoparticles, which are released into the bloodstream and trigger inflammatory responses in endothelial cells (54).

The subsequent discovery of HDP as a potent inducer of β-hematin formation provided an alternative candidate for this essential parasite pathway (42). Although no clear rationale has ever been given for examining this protein in this context, detailed biochemical studies have since aimed to elucidate the underlying reaction chemistry, resulting in a model in which specific histidine residues of HDP orient two hematin monomers to promote their dimerization (55-58).

Early localization studies using immunofluorescence and immuno-electron microscopy detected HDP in the host cell cytoplasm, hemoglobin transport vesicles, and the DV, consistent with a trafficking pathway involving secretion, export, and reuptake (42). When expressed episomally as a C-terminal GFP fusion, HDP localized to a tubular compartment within the parasite, interpreted as a hemoglobin trafficking intermediate (45). Support for a role in the DV came from Co-IP experiments showing that HDP associates with hemoglobin-degrading proteases, suggesting that they may act in concert with HDP to coordinate heme release and sequestration (44).

In our study, we tagged the endogenous HDP locus and found the protein to be associated with the parasite mitochondrion, colocalizing with both MitoTracker and a well-established mitochondrial reporter (59, 60). Low-level signals observed in the DV corresponded to natural background fluorescence, and even strong overexpression did not reveal any secondary protein pool. Since HDP is essential for parasite survival, the ability to tag the endogenous protein without compromising viability further supports that the observed localization reflects the physiological distribution of HDP. We found that the NTD of HDP is sufficient for mitochondrial targeting, whereas the N-termini of DV proteins typically direct them into the secretory pathway (61, 62). The most compelling support for HDP functioning exclusively in the mitochondrion comes from our observation that metabolically bypassing respiratory dysfunction fully restores the development of HDP-deficient parasites, along with normal hemozoin production.

The predicted structure of HDP indicates that two of the four histidine residues (H122 and H197), previously proposed to coordinate hematin binding (55), are deeply buried within the Fas1 fold, suggesting they are not accessible in solution (Figure 4B). Preparations of HDP retain their activity even after heating to >90°C, indicating that the protein's tertiary structure may not be critical for catalysis (42, 57). Circular dichroism spectroscopy, however, revealed some thermostability (42), in line with our observation of abnormal SDS-PAGE migration, which may reflect an inability to fully denature the tightly folded Fas1 domain. The catalytic role of HDP *in vitro* likely reflects the promiscuous nature of β-hematin formation, which can be greatly facilitated by nucleation centers supplied by proteins such as HDP and the HRPs, as well as by buffer components, impurities, certain lipids or ordered surfaces. Supporting this notion, studies in mice showed that loss of a lysosomal heme exporter leads to hemozoin deposits in reticuloendothelial macrophages that digest aged RBCs (63). Heme accumulation in acidic lysosomes is therefore sufficient to trigger biomineralization, even in organisms that do not normally form hemozoin, indicating that crystallization is chiefly driven by heme supersaturation and pH, with proteins, lipids, and small molecules only modulating the process. With HDP effectively disqualified, the only *Plasmodium*

369 protein currently known to affect hemozoin production *in cellulo* is PV5, a DV-localized lipocalin. Its
370 inactivation reduces hemozoin formation by approximately two-fold and causes excessive branching of
371 the crystals, with only mild effects on parasite viability (43).

372 Our comprehensive analysis of mitochondrial physiology demonstrates a role of HDP in
373 mitochondrial protein biosynthesis and mirrors previous observations made upon inactivation of the LSU
374 protein mRPL13 (64). Loss of HDP destabilizes the mitoribosome, thereby preventing the production of
375 key components of complexes III and IV. As a result, electron transport through the ETC is completely
376 blocked, abolishing the pH gradient required for $\Delta\Psi_{mt}$ maintenance and sensitizing the parasite to further
377 mitochondrial depolarization. Several lines of evidence support the notion that HDP is an integral part
378 of the mitoribosomal LSU: (1) despite notable differences in protein size and architecture, structural and
379 sequence alignments identify HDP as the most likely ortholog of the *T. gondii* LSU protein
380 TGME49_285272; (2) HDP inactivation selectively affects complexes whose integrity depends on
381 mitochondrial protein synthesis (19, 20); and (3) HDP inactivation compromises mitoribosome stability,
382 particularly within the LSU, where a predicted TGME49_285272 neighbor protein is most affected.

383 Although Co-IP-based identification of HDP binding partners would have been beneficial to
384 support an involvement in the LSU, this was severely hampered by the remarkable detergent resistance
385 of HDP. Even with heating and the use of high concentrations of dithiothreitol and sodium dodecyl
386 sulfate, the protein remained in the insoluble pellet and migrated abnormally during electrophoresis –
387 conditions that are not conducive to preserving native interactions. In the absence of such data, a
388 possible, though less likely, function for HDP could be the direct stabilization of complexes III and IV or
389 of their shared supercomplexes. Indeed, complexome profiling has revealed the presence of respiratory
390 supercomplexes in *P. falciparum* gametocytes, although their existence in asexual blood stages is less
391 clear (65). In *T. gondii*, supercomplexes of complexes III and IV have been observed, but disrupting the
392 underlying interactions caused only mild defects in parasite fitness and did not affect electron flow
393 through the ETC (66). In any case, a direct role for HDP in stabilizing the ETC would be difficult to
394 reconcile with the observed mitoribosomal destabilization.

395 In *T. gondii*, TGME49_285272 is located at the interface side of the LSU (21, 22). Available
396 structures of the mitoribosome resolved only 227 of the protein's 706 residues, covering the Fas1 core
397 but excluding the two loops emerging from the domain and lacking most of the extended NTD.
398 Interestingly, the resolved NTD residues are conserved in *P. falciparum*, spanning the entire NTD of
399 HDP except for the first eleven residues. This suggests that, despite holding targeting-relevant
400 information, the majority of the NTD remains intact following mitochondrial import. This is consistent with
401 observations in yeast, where approximately 25% of mitoribosomal proteins possess internal targeting
402 motifs that are not cleaved but are rich in positively charged and hydrophobic residues to facilitate import
403 (67). Our Western blot analysis, though limited by reduced protein solubilization, did not reveal clear
404 evidence of HDP processing, consistent with previous blots using HDP-specific antibodies (44, 57). A
405 stretch of the TGME49_285272 NTD corresponding to HDP residues 22-31 appears to align closely
406 with the rRNA LSUA in the *T. gondii* mitoribosome structure, suggesting a potential role in rRNA
407 stabilization (21, 22) (Figure 4K). The exact function of the Fas1 domain remains unclear, but it likely
408 contributes to stabilizing the overall LSU structure through its adhesive properties, consistent with the
409 widespread destabilization observed upon HDP loss. Indeed, a similar role has been shown for Fas1-
410 domain-containing linker proteins that stabilize light-harvesting complexes in algae (48).

411 Surprisingly, loss of HDP caused parasites to arrest development only in the second cycle, even
412 though complex IV subunits were already strongly reduced by the end of the first cycle. At that point,
413 $\Delta\Psi_{mt}$ remained intact, suggesting that despite the impact of HDP loss on the ETC, electron transport
414 was still sufficient to maintain $\Delta\Psi_{mt}$, or that processes dissipating the proton gradient had not yet taken
415 effect. Moreover, pyrimidine levels produced before mitochondrial dysfunction may have been enough
416 to sustain the parasites through one intraerythrocytic cycle, even after ubiquinone depletion caused
417 pyrimidine synthesis to halt. Parasites ultimately died at the trophozoite stage, when pyrimidine demand
418 reaches a critical level for the first round of DNA replication.

Together with its essential role in asexual blood-stage development, the divergent composition and structure of the apicomplexan mitoribosome highlights this unique protein-RNA assembly as an attractive target for future drug development (21, 22, 64, 68). Current antimalarial strategies already exploit selective inhibition of translation within the parasite's endosymbiotic organelles, with compounds such as doxycycline, clindamycin, and azithromycin targeting the apicoplast ribosomes (69-71). Secondary effects on mitochondrial translation have been observed, especially at higher concentrations (72-74), underscoring the mitoribosome's potential as a largely unexplored drug target. Elucidating the *Plasmodium* mitoribosome structure, as previously achieved for *T. gondii*, could pave the way for the rational design of inhibitors targeting the parasite's mitochondrial translation machinery. Such an approach would provide a powerful new avenue for antimalarial combination therapies that exploit synergy with established drugs acting on respiration, $\Delta\Psi_{mt}$ maintenance, or pyrimidine biosynthesis (68).

METHODS

Parasite cultivation and synchronization

P. falciparum blood stage parasites were cultured in deidentified human RBCs (B+; Universitätsklinikum Hamburg-Eppendorf) at 1-5% hematocrit in Roswell Park Memorial Institute medium 1640 (RPMI 1640) supplemented with 0.5% AlbuMAXII (Thermo Fisher Scientific) at 37°C under 1% O_2, 5% CO_2, and 94% N_2. For synchronization, mature schizonts were enriched by Percoll density gradient centrifugation and added to fresh RBCs for a 2-hour invasion under constant agitation. Residual schizonts were removed with a second Percoll gradient followed by 5% sorbitol treatment. For reverse genetic experiments, synchronized cultures were treated immediately with 20 nM RAP (Clontech Laboratories) or DMSO (Merck).

Generation and validation of transgenic parasites

For editing of the HDP locus (PF3D7_1446800), DiCre-expressing *P. falciparum* schizonts (strain: B11) (75) were transfected with 20 µg of guide plasmid to induce Cas9-mediated double strand cleavage, together with 60 µg of linearized repair template, using a 4D Nucleofector system (Lonza). The repair template was generated by commercial gene synthesis, contained 5′ and 3′ homology regions and a recodonized HDP sequence with two *loxP* sites – one within an artificial intron and one downstream of the stop codon (46). mNG was cloned in-frame using HpaI and EcoRV restriction sites. Transgenic parasites were selected with 10 nM WR99210 (Jacobus Pharmaceuticals) and cloned by limiting dilution. Correct genomic integration and RAP-induced excision were confirmed by diagnostic PCR and fluorescence microscopy.

Endogenous tagging of Cox5B (PF3D7_0927800) and NDUFA4 (PF3D7_1439600) was achieved using the selection-linked integration system (76). Tagging vectors were derived from the pSLI-PF3D7_1476700-mNeonGreen-glmS plasmid (77) and generated by first replacing mNG with mCh using the MluI and SalI sites, followed by cloning of the respective C-terminal region in frame with mCh using the NotI and MluI sites. After transfection, parasites were selected with WR99210 until resistant populations emerged and then treated with 0.4 mM neomycin (Merck) to enrich for integrants. Plasmids for episomal expression of the apicoplast (78) and mitochondrial (60) markers were maintained using 2 µg/mL blasticidin S (Thermo Fisher Scientific) or 0.9 µM DSM1 (Merck), respectively. The episomal construct driving NTD-mCh expression was generated by replacing the citrate synthase leader sequence in the mitochondrial marker plasmid pNMD3:Mito-mCherry-DHODH (60) with the first 48 residues of HDP, using the XhoI and KpnI sites.

All transgenic parasite lines generated in this study are listed in Supplementary Table S3, and primers for molecular cloning, guide plasmid construction, diagnostic PCR, and the repair template sequence are provided in Supplementary Table S2.

Western blotting

For Western blot analysis, parasites were released from their host cells by treatment with 0.03% saponin in PBS. Parasites were then pelleted and lysed in 0.5 x PBS containing 4% SDS, 0.5% Triton X-100 and protease inhibitor cocktail (Roche). After one freeze-thaw cycle, the lysate was centrifuged at 21,130 x g for 10 minutes. The supernatant and pellet fractions were taken up in 5x Laemmli buffer containing 0.6 M dithiothreitol, heated to 85°C for 5 minutes, and subjected to SDS-PAGE. Following transfer onto nitrocellulose membranes and blocking with milk, primary antibodies were applied at the following concentrations: α-BiP (rabbit, 1:2,000) (79), α-mNG (ChromoTek, mouse, 1:1,000), α-RFP (ChromoTek, rat, 1:1,000). Bound primary antibodies were detected by chemiluminescence using horseradish-peroxidase-conjugated secondary antibodies (Agilent, 1:5,000 - 1:3,000) and ECL reagent.

474 **Parasite replication and drug sensitivity assays**

475 As described previously (80), growth assays were initiated with synchronized ring-stage cultures
476 adjusted to a parasitemia of 0.1% and supplemented with DMSO, RAP and/or 25 µM dQ (Cayman
477 Chemical). Parasitemia was quantified every two days over four replication cycles by flow cytometry.
478 For this, parasites were stained for 40 minutes at 37°C in medium containing SYBR Green nuclear dye
479 (1:10,000; Thermo Fisher Scientific), followed by a 40-minute de-staining period. The proportion of
480 stained cells was then measured on an automated NovoCyte 3000VYB flow cytometer equipped with a
481 NovoSampler Pro (Agilent).

482 To analyze parasite drug sensitivity, synchronized *hdp-mNG:loxP* + *ydhodh* parasite cultures
483 were adjusted to 0.1% parasitemia at 2% hematocrit and incubated in 96-well black-bottom plates
484 (Thermo Fisher Scientific) with DMSO or RAP and varying concentrations of chloroquine or proguanil
485 (both from Merck) in a final volume of 200 µl. Parasites were lysed 120 hours post-invasion, and DNA
486 was stained with SYBR Gold (Invitrogen), as described previously (81). Fluorescence was measured
487 using a GENios plate reader (Tecan), with excitation and emission wavelengths set to 485 nm and 535
488 nm, respectively. Raw fluorescence values were corrected using non-infected RBC controls and
489 normalized to the highest and lowest readings.

490 **Microscopy**

491 All light and fluorescence microscopy was performed on a DM6 B microscope equipped with a
492 K8 B/W camera and a K3C color camera (all from Leica). The microscope was fitted with two crossed
493 polarizers to enable selective visualization of hemozoin. For quantification of parasite size and hemozoin
494 content, methanol-fixed blood smears were recorded in the DIC and polarization channels. RBC and
495 parasite were manually outlined, and their areas measured. Hemozoin clusters were delineated in the
496 polarization channel using manual thresholding, and their raw integrated densities were measured and
497 corrected for background.

498 To assess $\Delta\Psi_{mt}$, cells were stained at 37°C for 30 minutes in medium containing 2.5 nM
499 MitoTracker Red CMXRos (Invitrogen), with or without 250 µM FCCP (Merck). After 30 additional
500 minutes of de-staining, parasites were then imaged, and mitochondria were outlined using manual
501 thresholding to determine background-corrected mean fluorescence intensity. Vacuolar
502 autofluorescence was quantified by measuring background-corrected raw integrated density in manually
503 outlined DVs, excluding parasites in which the mitochondrion was in close proximity to the DV.

504 To examine crystal morphology, hemozoin was isolated from 36-hour-old *hdp-mNG:loxP* +
505 *ydhodh* parasites in the second cycle post-induction, as described previously (43). Parasites were lysed
506 in 2% SDS, and the lysate was centrifuged at 21,130 x g for 5 minutes. The resulting pellet was washed
507 twice in 2% SDS and three times with distilled water. Crystals were transferred onto 12 mm round glass
508 coverslips and allowed to dry. Coverslips were then mounted on specimen stubs, sputter-coated with 5
509 nm gold using a CCU-010 compact coating unit (safematic), and then imaged using a CLARA scanning
510 electron microscope (Tescan) at 5 keV.

511 **Extracellular flux analysis**

512 For Seahorse assays, 30 mL cultures containing young schizonts at >3% parasitemia and 4%
513 hematocrit were collected in the second cycle post-induction. Parasites were released from their host
514 cells by incubation in PBS containing 0.05-0.15% saponin (Merck). The isolated parasites were washed
515 twice in PBS and resuspended in Mitochondria Assay Solution (MAS; 220 mM mannitol, 70 mM sucrose,
516 10 mM KH_2PO_4, 5 mM $MgCl_2$, 2 mM HEPES, and 1 mM EGTA, adjusted to pH 7.2), supplemented with
517 2 mg/mL fatty acid-free bovine serum albumin, 24 mM malate, and 0.1 % v/v DMSO (all from Merck).

518 Parasites were counted using a Neubauer chamber and resuspended at 5 x 10^7 cells per mL in
519 supplemented MAS further containing 0.002% w/v digitonin (Merck), as described previously (60, 82).

520 OCR was measured on a Seahorse XFe96 Analyzer using Wave software (Agilent). For each
521 well, 5 x 10^6 parasites were loaded into CellTak-coated plates (Corning) and allowed to adhere by gentle
522 centrifugation at 800 x g for 10 minutes. Even distribution and equal parasite density were confirmed
523 microscopically. The assay included a total of 12 measurement cycles, each consisting of 3 minutes of
524 mixing followed by 3 minutes of measuring. Three cycles were recorded sequentially for each step: first
525 to assess basal respiration, then following the injection of 5 µM atovaquone, next after the addition of
526 0.2 mM TMPD with 2 mM ascorbate, and finally after 10 mM sodium azide (all from Merck). Assays
527 were repeated with 6 independent parasite preparations, each comprising 6-30 technical replicates per
528 condition, depending on cell yield.

529 **Label-free quantitative mass spectrometry**

530 For whole-proteome profiling, 50 mL of DMSO- and RAP-treated *hdp-mNG:loxP* + *ydhodh* ring-
531 stage cultures were adjusted to a parasitemia of 1.5% and a hematocrit of 2%, then harvested 80 hours
532 post-invasion. Parasites were released from RBCs by a 10-minute incubation in ice-cold PBS containing
533 0.03% saponin, pelleted, and washed twice in the same buffer. Freed parasites were washed three
534 additional times in ice-cold PBS. After a final centrifugation, the supernatant was removed and the
535 parasite pellets were snap frozen in liquid N_2 for 30 seconds and subsequently stored at -70°C. Parasite
536 proteins were isolated, digested with trypsin, and analyzed by liquid chromatography – mass
537 spectrometry (LC-MS), as described in the Supplementary Methods.

538 **Statistical analysis and software**

539 Statistical analyses were performed using GraphPad Prism (version 10.4.1). Comparisons
540 between DMSO- and RAP-treated conditions were evaluated using paired t-tests, whereas comparisons
541 between independent variables were assessed with unpaired t-tests. Growth curves were analyzed by
542 two-way ANOVA. For imaging-based experiments, statistical tests were applied to the mean values of
543 independent biological replicates rather than to individual parasites. IC_{50} values were calculated by non-
544 linear regression using the "log(inhibitor) vs. response – Variable slope (four parameters)" model.

545 Raw mass spectrometry data were processed using DIA-NN (version 2.2.0, see Supplementary
546 Methods) (87). Proteins were included in the final datasets only if identified by at least two peptides.
547 Statistical analysis was performed using Student's t-test with Benjamini-Hochberg correction, controlling
548 the false discovery rate at 1%. Proteins were considered differentially expressed if they showed a $\log_2$
549 fold-change ≥ 0.5 or ≤ -0.5, an adjusted p-value ≤ 0.01, and were detected in more than 75% of runs in
550 at least one condition. Combined reduction scores were calculated as the $\log_2$ fold-change multiplied by
551 the negative $\log_{10}$ of the p-value.

552 Microscopy images were analyzed and processed using FIJI (version 2.16.0/1.54p). Structural
553 models of HDP and Fas1-domain-containing proteins of *T. gondii*, as well as individual Fas1 domains,
554 were generated using the AlphaFold 3 server (49). Structures were visualized and aligned using PyMOL
555 (version 2.5.7) and ChimeraX (version 1.10). Multiple sequence alignments were performed with Clustal
556 Omega (83). Graphs were generated using Prism, and final figures were assembled in Adobe Illustrator
557 (version 28.0.0.88).

558 **Data, materials, and software availability**

559 All study data are included in the article and its supplementary materials. DNA constructs and
560 transgenic parasite lines used in this study are available upon reasonable request.

REFERENCES

1. H. Fischer, Synthese des Hämins. *Naturwiss* **17**, 611-617 (1929).
2. T. Shimizu, A. Lengalova, V. Martinek, M. Martinkova, Heme: emergent roles of heme in signal transduction, functional regulation and as catalytic centres. *Chem Soc Rev* **48**, 5624-5657 (2019).
3. M. Paoli, J. Marles-Wright, A. Smith, Structure-function relationships in heme-proteins. *DNA Cell Biol* **21**, 271-280 (2002).
4. T. L. Poulos, Heme enzyme structure and function. *Chem Rev* **114**, 3919-3962 (2014).
5. C. C. Murdoch, E. P. Skaar, Nutritional immunity: the battle for nutrient metals at the host-pathogen interface. *Nat Rev Microbiol* **20**, 657-670 (2022).
6. A. G. Maier, K. Matuschewski, M. Zhang, M. Rug, *Plasmodium falciparum*. *Trends Parasitol* **35**, 481-482 (2019).
7. H. Ke *et al.*, The heme biosynthesis pathway is essential for *Plasmodium falciparum* development in mosquito stage but not in blood stages. *J Biol Chem* **289**, 34827-34837 (2014).
8. Z. Rizopoulos, K. Matuschewski, J. M. Haussig, Distinct prominent roles for enzymes of *Plasmodium berghei* heme biosynthesis in sporozoite and liver stage maturation. *Infect Immun* **84**, 3252-3262 (2016).
9. V. A. Nagaraj *et al.*, Malaria parasite-synthesized heme is essential in the mosquito and liver stages and complements host heme in the blood stages of infection. *PLoS Pathog* **9**, e1003522 (2013).
10. H. J. Painter, J. M. Morrisey, M. W. Mather, A. B. Vaidya, Specific role of mitochondrial electron transport in blood-stage *Plasmodium falciparum*. *Nature* **446**, 88-91 (2007).
11. H. Ke *et al.*, Genetic investigation of tricarboxylic acid metabolism during the *Plasmodium falciparum* life cycle. *Cell Rep* **11**, 164-174 (2015).
12. K. Rajaram, S. G. Tewari, A. Wallqvist, S. T. Prigge, Metabolic changes accompanying the loss of fumarate hydratase and malate-quinone oxidoreductase in the asexual blood stage of *Plasmodium falciparum*. *J Biol Chem* **298**, 101897 (2022).
13. A. Sturm, V. Mollard, A. Cozijnsen, C. D. Goodman, G. I. McFadden, Mitochondrial ATP synthase is dispensable in blood-stage *Plasmodium berghei* rodent malaria but essential in the mosquito phase. *Proc Natl Acad Sci U S A* **112**, 10216-10223 (2015).
14. E. Bushell *et al.*, Functional profiling of a *Plasmodium* genome reveals an abundance of essential genes. *Cell* **170**, 260-272 e268 (2017).
15. M. Zhang *et al.*, Uncovering the essential genes of the human malaria parasite *Plasmodium falciparum* by saturation mutagenesis. *Science* **360** (2018).
16. M. Fry, E. Webb, M. Pudney, Effect of mitochondrial inhibitors on adenosinetriphosphate levels in *Plasmodium falciparum*. *Comp Biochem Physiol B* **96**, 775-782 (1990).
17. S. A. Uyemura, S. Luo, M. Vieira, S. N. Moreno, R. Docampo, Oxidative phosphorylation and rotenone-insensitive malate- and NADH-quinone oxidoreductases in *Plasmodium yoelii yoelii* mitochondria *in situ*. *J Biol Chem* **279**, 385-393 (2004).
18. A. A. Divo, T. G. Geary, J. B. Jensen, H. Ginsburg, The mitochondrion of *Plasmodium falciparum* visualized by rhodamine 123 fluorescence. *J Protozool* **32**, 442-446 (1985).
19. J. E. Feagin, M. J. Gardner, D. H. Williamson, R. J. Wilson, The putative mitochondrial genome of *Plasmodium falciparum*. *J Protozool* **38**, 243-245 (1991).
20. J. E. Feagin, B. L. Mericle, E. Werner, M. Morris, Identification of additional rRNA fragments encoded by the P*lasmodium falciparum* 6 kb element. *Nucleic Acids Res* **25**, 438-446 (1997).
21. S. Shikha *et al.*, Numerous rRNA molecules form the apicomplexan mitoribosome via repurposed protein and RNA elements. *Nat Commun* **16**, 817 (2025).
22. C. Wang *et al.*, Apicomplexan mitoribosome from highly fragmented rRNAs to a functional machine. *Nat Commun* **15**, 10689 (2024).
23. J. E. Siregar *et al.*, Direct evidence for the atovaquone action on the *Plasmodium* cytochrome bc_1 complex. *Parasitol Int* **64**, 295-300 (2015).
24. M. W. Mather *et al.*, Uncovering the molecular mode of action of the antimalarial drug atovaquone using a bacterial system. *J Biol Chem* **280**, 27458-27465 (2005).
25. H. Ke *et al.*, Mitochondrial type II NADH dehydrogenase of *Plasmodium falciparum* (*Pf*NDH2) is dispensable in the asexual blood stages. *PLoS One* **14**, e0214023 (2019).
26. K. E. Boysen, K. Matuschewski, Arrested oocyst maturation in *Plasmodium* parasites lacking type II NADH:ubiquinone dehydrogenase. *J Biol Chem* **286**, 32661-32671 (2011).

27. H. Ke *et al.*, Variation among *Plasmodium falciparum* strains in their reliance on mitochondrial electron transport chain function. *Eukaryot Cell* **10**, 1053-1061 (2011).

28. J. M. Matz, *Plasmodium*'s bottomless pit: properties and functions of the malaria parasite's digestive vacuole. *Trends Parasitol* **38**, 525-543 (2022).

29. S. Kumar, U. Bandyopadhyay, Free heme toxicity and its detoxification systems in human. *Toxicol Lett* **157**, 175-188 (2005).

30. S. Azouzi, K. El Kirat, S. Morandat, Hematin loses its membranotropic activity upon oligomerization into malaria pigment. *Biochim Biophys Acta* **1848**, 2952-2959 (2015).

31. T. J. Egan *et al.*, Fate of haem iron in the malaria parasite *Plasmodium falciparum*. *Biochem J* **365**, 343-347 (2002).

32. S. Pagola, P. W. Stephens, D. S. Bohle, A. D. Kosar, S. K. Madsen, The structure of malaria pigment beta-haematin. *Nature* **404**, 307-310 (2000).

33. J. M. Combrinck *et al.*, Insights into the role of heme in the mechanism of action of antimalarials. *ACS Chem Biol* **8**, 133-137 (2013).

34. D. J. Sullivan, Jr., I. Y. Gluzman, D. G. Russell, D. E. Goldberg, On the molecular mechanism of chloroquine's antimalarial action. *Proc Natl Acad Sci U S A* **93**, 11865-11870 (1996).

35. K. N. Olafson, M. A. Ketchum, J. D. Rimer, P. G. Vekilov, Mechanisms of hematin crystallization and inhibition by the antimalarial drug chloroquine. *Proc Natl Acad Sci U S A* **112**, 4946-4951 (2015).

36. K. N. Olafson, T. Q. Nguyen, J. D. Rimer, P. G. Vekilov, Antimalarials inhibit hematin crystallization by unique drug-surface site interactions. *Proc Natl Acad Sci U S A* **114**, 7531-7536 (2017).

37. J. M. Pisciotta *et al.*, The role of neutral lipid nanospheres in *Plasmodium falciparum* haem crystallization. *Biochem J* **402**, 197-204 (2007).

38. M. A. Ambele, T. J. Egan, Neutral lipids associated with haemozoin mediate efficient and rapid beta-haematin formation at physiological pH, temperature and ionic composition. *Malar J* **11**, 337 (2012).

39. N. T. Huy *et al.*, Phospholipid membrane-mediated hemozoin formation: the effects of physical properties and evidence of membrane surrounding hemozoin. *PLoS One* **8**, e70025 (2013).

40. A. N. Hoang, K. K. Ncokazi, K. A. de Villiers, D. W. Wright, T. J. Egan, Crystallization of synthetic haemozoin (beta-haematin) nucleated at the surface of lipid particles. *Dalton Trans* **39**, 1235-1244 (2010).

41. D. J. Sullivan, Jr., I. Y. Gluzman, D. E. Goldberg, *Plasmodium* hemozoin formation mediated by histidine-rich proteins. *Science* **271**, 219-222 (1996).

42. D. Jani *et al.*, HDP - a novel heme detoxification protein from the malaria parasite. *PLoS Pathog* **4**, e1000053 (2008).

43. J. M. Matz *et al.*, A lipocalin mediates unidirectional heme biomineralization in malaria parasites. *Proc Natl Acad Sci U S A* **117**, 16546-16556 (2020).

44. M. Chugh *et al.*, Protein complex directs hemoglobin-to-hemozoin formation in *Plasmodium falciparum*. *Proc Natl Acad Sci U S A* **110**, 5392-5397 (2013).

45. P. Gupta *et al.*, Heme detoxification protein (*Pf*HDP) is essential for the hemoglobin uptake and metabolism in *Plasmodium falciparum*. *FASEB Bioadv* **4**, 662-674 (2022).

46. E. Knuepfer, M. Napiorkowska, C. van Ooij, A. A. Holder, Generating conditional gene knockouts in *Plasmodium* - a toolkit to produce stable DiCre recombinase-expressing parasite lines using CRISPR/Cas9. *Sci Rep* **7**, 3881 (2017).

47. G. J. Seifert, Fascinating fasciclins: a surprisingly widespread family of proteins that mediate interactions between the cell exterior and the cell surface. *Int J Mol Sci* **19** (2018).

48. J. Zhang *et al.*, Structure of phycobilisome from the red alga *Griffithsia pacifica*. *Nature* **551**, 57-63 (2017).

49. J. Abramson *et al.*, Accurate structure prediction of biomolecular interactions with AlphaFold 3. *Nature* **630**, 493-500 (2024).

50. J. Underhaug *et al.*, Mutation in transforming growth factor beta induced protein associated with granular corneal dystrophy type 1 reduces the proteolytic susceptibility through local structural stabilization. *Biochim Biophys Acta* **1834**, 2812-2822 (2013).

51. R. Virchow, Zur pathologischen Physiologie des Bluts. *Arch Pathol Anatomie* **2**, 587-598 (1849).

52. C. L. Laveran, Note sur un nouveau parasite trouvé dans le sang de plusieurs malades atteints de fièvre palustre. *Bull Acad Méd* **9**, 1235-1236 (1880).

53. A. U. Orjih, Heme polymerase activity and the stage specificity of antimalarial action of chloroquine. *J Pharmacol Exp Ther* **282**, 108-112 (1997).

54. S. T. Nguyen *et al.*, Histidine-rich protein II nanoparticle delivery of heme iron load drives endothelial inflammation in cerebral malaria. *Proc Natl Acad Sci U S A* **120**, e2306318120 (2023).

671 55. K. Nakatani, H. Ishikawa, S. Aono, Y. Mizutani, Identification of essential histidine residues involved in
672 heme binding and hemozoin formation in heme detoxification protein from *Plasmodium falciparum*. *Sci*
673 *Rep* **4**, 6137 (2014).

674 56. K. Nakatani, H. Ishikawa, S. Aono, Y. Mizutani, Heme-binding properties of heme detoxification protein
675 from *Plasmodium falciparum*. *Biochem Biophys Res Commun* **439**, 477-480 (2013).

676 57. A. Soni *et al.*, Cloning, expression and functional characterization of heme detoxification protein (HDP)
677 from the rodent malaria parasite *Plasmodium vinckei*. *Gene* **566**, 109-119 (2015).

678 58. P. Gupta *et al.*, Exploring heme and hemoglobin binding regions of *Plasmodium* heme detoxification
679 protein for new antimalarial discovery. *J Med Chem* **60**, 8298-8308 (2017).

680 59. C. J. Tonkin *et al.*, Localization of organellar proteins in *Plasmodium falciparum* using a novel set of
681 transfection vectors and a new immunofluorescence fixation method. *Mol Biochem Parasitol* **137**, 13-21
682 (2004).

683 60. E. Pietsch *et al.*, A patatin-like phospholipase is important for mitochondrial function in malaria parasites.
684 *mBio* **14**, e0171823 (2023).

685 61. M. Klemba, W. Beatty, I. Gluzman, D. E. Goldberg, Trafficking of plasmepsin II to the food vacuole of the
686 malaria parasite *Plasmodium falciparum*. *J Cell Biol* **164**, 47-56 (2004).

687 62. P. V. Dasaradhi *et al.*, Food vacuole targeting and trafficking of falcipain-2, an important cysteine protease
688 of human malaria parasite *Plasmodium falciparum*. *Mol Biochem Parasitol* **156**, 12-23 (2007).

689 63. R. H. Pek *et al.*, Hemozoin produced by mammals confers heme tolerance. *Elife* **8** (2019).

690 64. H. Ke, S. Dass, J. M. Morrisey, M. W. Mather, A. B. Vaidya, The mitochondrial ribosomal protein L13 is
691 critical for the structural and functional integrity of the mitochondrion in *Plasmodium falciparum*. *J Biol*
692 *Chem* **293**, 8128-8137 (2018).

693 65. F. Evers *et al.*, Composition and stage dynamics of mitochondrial complexes in *Plasmodium falciparum*.
694 *Nat Commun* **12**, 3820 (2021).

695 66. A. E. MacLean *et al.*, Structure, assembly and inhibition of the *Toxoplasma gondii* respiratory chain
696 supercomplex. *Nat Struct Mol Biol* **32**, 1424-1433 (2025).

697 67. Y. S. Bykov *et al.*, Widespread use of unconventional targeting signals in mitochondrial ribosome proteins.
698 *EMBO J* **41**, e109519 (2022).

699 68. L. Ling *et al.*, Genetic ablation of the mitoribosome in the malaria parasite *Plasmodium falciparum*
700 sensitizes it to antimalarials that target mitochondrial functions. *J Biol Chem* **295**, 7235-7248 (2020).

701 69. E. L. Dahl *et al.*, Tetracyclines specifically target the apicoplast of the malaria parasite *Plasmodium*
702 *falciparum*. *Antimicrob Agents Chemother* **50**, 3124-3131 (2006).

703 70. M. Camps, G. Arrizabalaga, J. Boothroyd, An rRNA mutation identifies the apicoplast as the target for
704 clindamycin in *Toxoplasma gondii*. *Mol Microbiol* **43**, 1309-1318 (2002).

705 71. A. B. Sidhu *et al.*, *In vitro* efficacy, resistance selection, and structural modeling studies implicate the
706 malarial parasite apicoplast as the target of azithromycin. *J Biol Chem* **282**, 2494-2504 (2007).

707 72. M. Okada, P. Guo, S. A. Nalder, P. A. Sigala, Doxycycline has distinct apicoplast-specific mechanisms of
708 antimalarial activity. *Elife* **9** (2020).

709 73. R. Kiatfuengfoo, T. Suthiphongchai, P. Prapunwattana, Y. Yuthavong, Mitochondria as the site of action
710 of tetracycline on *Plasmodium falciparum*. *Mol Biochem Parasitol* **34**, 109-115 (1989).

711 74. Q. Lin, K. Katakura, M. Suzuki, Inhibition of mitochondrial and plastid activity of *Plasmodium falciparum*
712 by minocycline. *FEBS Lett* **515**, 71-74 (2002).

713 75. A. J. Perrin *et al.*, The actinomyosin motor drives malaria parasite red blood cell invasion but not egress.
714 *mBio* **9**, e00905-00918 (2018).

715 76. J. Birnbaum *et al.*, A genetic system to study *Plasmodium falciparum* protein function. *Nat Methods* **14**,
716 450-456 (2017).

717 77. E. Pietsch *et al.*, Disruption of a *Plasmodium falciparum* patatin-like phospholipase delays male
718 gametocyte exflagellation. *Mol Microbiol* **121**, 529-542 (2024).

719 78. J. Birnbaum *et al.*, A Kelch13-defined endocytosis pathway mediates artemisinin resistance in malaria
720 parasites. *Science* **367**, 51-59 (2020).

721 79. E. Knuepfer *et al.*, RON12, a novel *Plasmodium*-specific rhoptry neck protein important for parasite
722 proliferation. *Cell Microbiol* **16**, 657-672 (2014).

723 80. A. Alder *et al.*, The role of *Plasmodium* V-ATPase in vacuolar physiology and antimalarial drug uptake.
724 *Proc Natl Acad Sci U S A* **120**, e2306420120 (2023).

725 81. A. Alder *et al.*, A non-reactive natural product precursor of the duocarmycin family has potent and selective
726 antimalarial activity. *Cell Chem Biol* **29**, 840-853 (2021).

82. S. Ramesh, D. Cihalova, E. Rajendran, G. G. Van Dooren, A. G. Maier, Analysis of *Plasmodium falciparum* mitochondrial electron transport chain activity using Seahorse XFe96 extracellular flux assays. *Bio Protoc* **13**, e4863 (2023).

83. F. Sievers *et al.*, Fast, scalable generation of high-quality protein multiple sequence alignments using Clustal Omega. *Mol Syst Biol* **7**, 539 (2011).

84. J. R. Wisniewski, A. Zougman, N. Nagaraj, M. Mann, Universal sample preparation method for proteome analysis. *Nat Methods* **6**, 359-362 (2009).

85. U. Distler, J. Kuharev, P. Navarro, S. Tenzer, Label-free quantification in ion mobility-enhanced data-independent acquisition proteomics. *Nat Protoc* **11**, 795-812 (2016).

86. F. Meier *et al.*, diaPASEF: parallel accumulation-serial fragmentation combined with data-independent acquisition. *Nat Methods* **17**, 1229-1236 (2020).

87. V. Demichev, C. B. Messner, S. I. Vernardis, K. S. Lilley, M. Ralser, DIA-NN: neural networks and interference correction enable deep proteome coverage in high throughput. *Nat Methods* **17**, 41-44 (2020).

ACKNOWLEDGEMENTS

We thank Mathieu Brochet and Dominique Soldati-Favre from the Université de Genève for access to the research infrastructures required for cellular bioenergetics analysis, and Paul-Christian Burda from the Justus Liebig University Giessen for providing plasmids used in this study. This work was funded by the Bundesministerium für Forschung, Technologie und Raumfahrt (BMFTR; Federal Ministry of Research, Technology and Space; grant number 01KI2104 to JMM). Responsibility for the content of this publication lies solely with the authors. We also acknowledge financial support from the priority program SPP 2225 “Exit Strategies of Intracellular Pathogens” of the Deutsche Forschungsgemeinschaft (DFG; German Research Foundation; projects 531646514 to JMM and 446605368 to UD). LS is supported by a stipend from the Jürgen Manchot Stiftung. CB is the recipient of a Swiss Postdoctoral Fellowship from the Schweizer Nationalfonds (Swiss National Science Foundation, project 217028). JK receives funding from a generous donor advised by CARIGEST SA, acquired by Dominique Soldati-Favre.

AUTHOR CONTRIBUTIONS

Conceptualization: JMM
Methodology: LS, JK, TZ, KSH, UD, JMM
Investigation: LS, JK, TZ, YS, ALS, RDE, KSH, CB
Data Curation and Analysis: LS, JK, TZ, UD, JMM
Funding Acquisition: LS, UD, CB, JMM
Writing – Original Draft: LS, JMM
Writing – Review & Editing: all authors

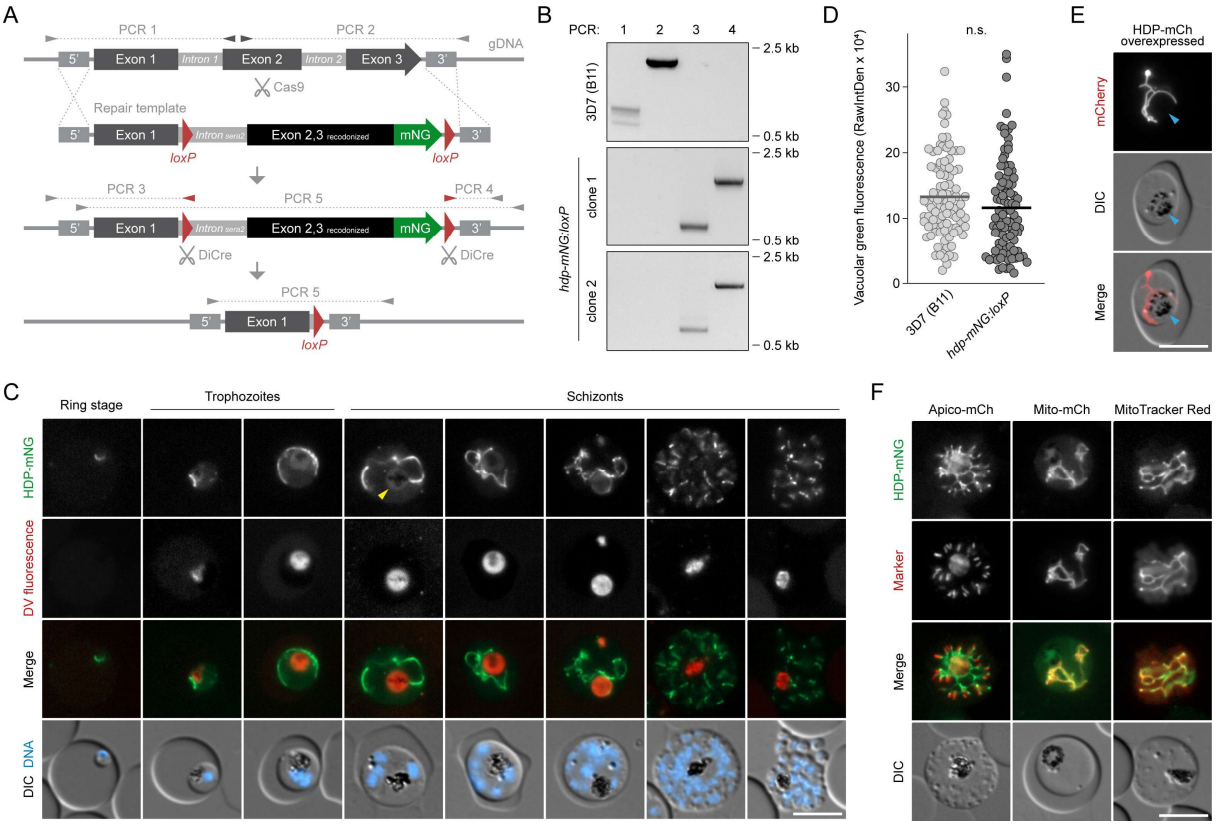

Figure 1: HDP localizes to the parasite mitochondrion.

(A) Genetic strategy for tagging and conditional deletion of HDP using Cas9 and the DiCre system. Shown are the endogenous locus, the synthetic repair template, and the recombined locus before and after excision. Primer combinations for diagnostic PCRs are indicated.

(B) Diagnostic PCRs as in (A), using genomic DNA isolated from the parental line and two independent *hdp-mNG:loxP* clones.

(C) Expression and localization of HDP-mNG observed by live fluorescence microscopy. Representative images are shown throughout the intraerythrocytic cycle. The DV was visualized via porphyrin-derived autofluorescence. Yellow arrowhead: faint signal in the DV.

(D) Green DV fluorescence in *hdp-mNG:loxP* parasites does not exceed the background observed in parental parasites 36 hours post-invasion. Shown are mean and individual values. n.s., non-significant, paired t-test; N = 99 parasites from 3 independent experiments.

(E) Overexpressed HDP-mCh localizes exclusively to a branching organelle. Blue arrowheads: position of the DV.

(F) HDP-mNG colocalizes with mitochondrial markers. Shown are *hdp-mNG:loxP* parasites expressing fluorescent organelle markers (Apico-mCh, Mito-mCh) or stained with MitoTracker Red CMXRos. Scale bars, 5 µm.

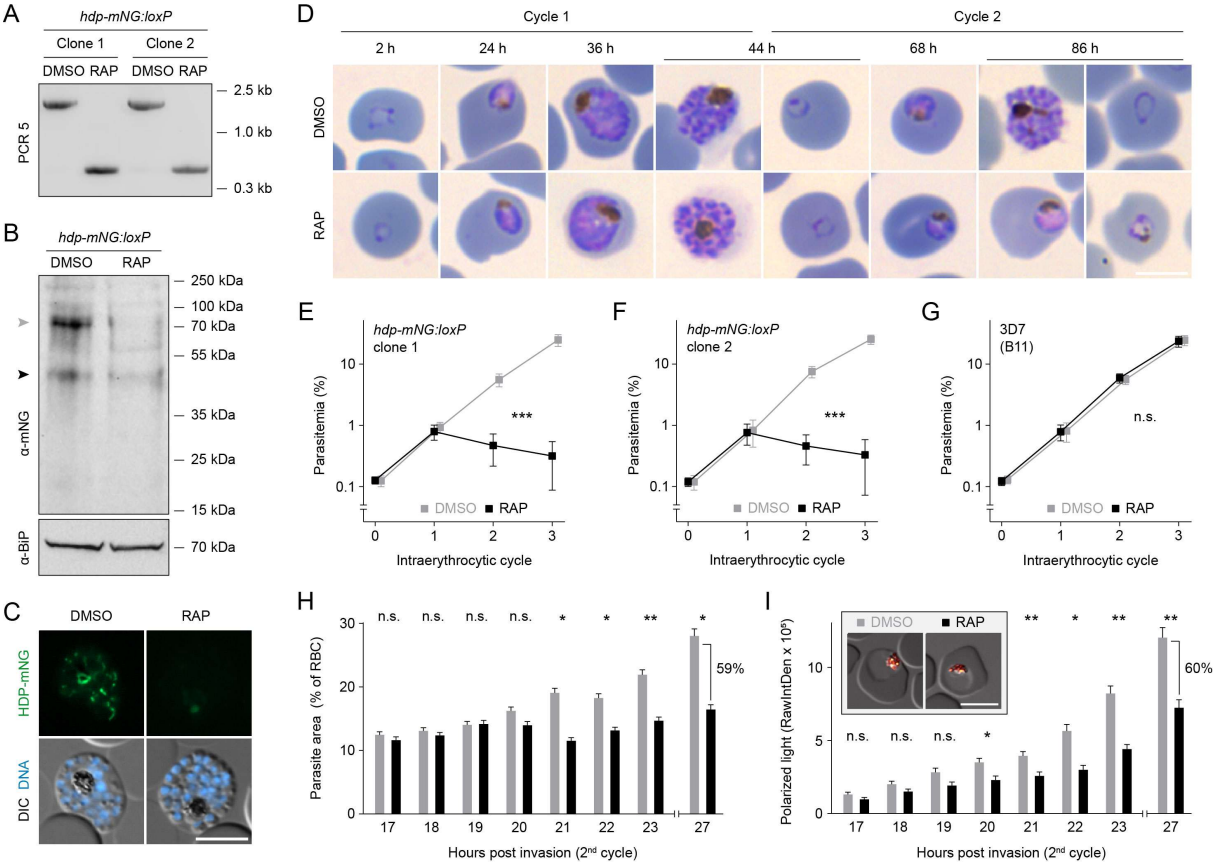

Figure 2: Loss of HDP causes developmental arrest accompanied by reduced hemozoin content.

(A-C) RAP-induced loss of HDP, as confirmed by (A) diagnostic PCR5 (see Figure 1A), (B) Western blot, and (C) live cell imaging at the end of the first cycle. Black arrowhead: predicted size of HDP-mNG; grey arrowhead: higher molecular weight band.

(D) HDP-deficient parasites arrest as trophozoites during the second cycle following RAP treatment, as shown by Giemsa staining.

(E-G) HDP-deficient parasites fail to replicate beyond the second cycle. Growth curves are shown for two independent DMSO and RAP-treated *hdp-mNG:loxP* clones (E, F) and parental parasites (G). Shown are mean values +/- SD. n.s., non-significant; ***P<0.001, two-way ANOVA; N = 3 biological replicates with 3 technical replicates each.

(H, I) Quantification of parasite size (H) and hemozoin content (I) demonstrates a tight temporal correlation between growth arrest and reduced hemozoin production. Hemozoin was quantified by polarization microscopy. Shown are mean values + SEM. *P<0.05, **P<0.01, paired t-test; N = 99 parasites from 3 independent experiments. Inset: parasites 27 hours post-invasion, shown as a merge of DIC (grey) and polarized light (orange). Scale bars, 5 µm.

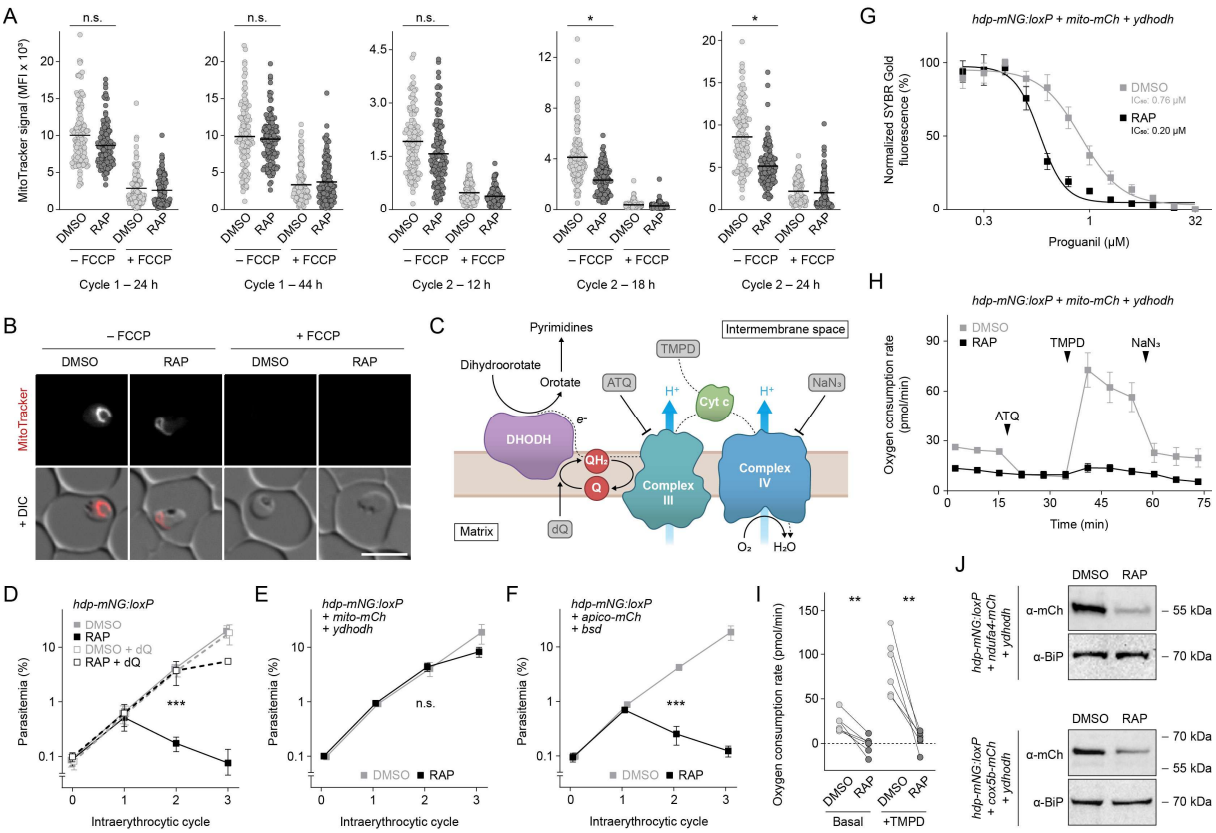

Figure 3: HDP is essential for mitochondrial electron transport.

(A, B) Loss of HDP dissipates $\Delta\Psi_{mt}$. (A) Live microscopy of Mitotracker Red CMXRos staining was used to quantify $\Delta\Psi_{mt}$ in the presence or absence of FCCP at the indicated timepoints. Mean and individual values are shown. n.s., non-significant; *P<0.05, paired t-test; N = 132 parasites from 4 independent experiments. (B) Representative microscopy images at 18 hours post-invasion in the second cycle. Scale bar, 5 µm.

(C) Schematic representation of respiratory complexes III and IV and their role in pyrimidine biosynthesis. Exogenous compounds are shown in grey. DHODH, dihydroorotate dehydrogenase; Cyt c, cytochrome c; Q, ubiquinone; QH_2, ubiquinol; dQ, decyl-ubiquinone; ATQ, atovaquone; TMPD, N,N,N′,N′-Tetramethyl-1,4-phenylendiamin; NaN_3, sodium azide.

(D-F) HDP-deficient parasites are rescued by exogenous dQ (D) or expression of yeast DHODH (yDHODH) (E), but not by expression of blasticidin S deaminase (BSD) (F). Growth curves show mean values +/- SD. ***P<0.001, two-way ANOVA; N = 3 biological replicates with 3 technical replicates each.

(G) HDP-deficient parasites are hypersensitive to proguanil. Growth-response curves of yDHODH-rescued parasites are shown, with mean +/- SEM and IC_{50} values indicated. N = 3 biological replicates with 3 technical replicates each.

(H, I) Loss of HDP disrupts respiration. (H) Oxygen consumption rate (OCR) of yDHODH-rescued parasites over the course of one Seahorse assay. Timepoints for compound addition are indicated. Shown are mean values +/- SEM. (I) OCR under basal conditions and in the presence of TMPD. Individual values are shown. **P<0.01, paired t-test; N = 6 assays with ≥ 6 technical replicates each.

814 **(J)** HDP-deficient parasites show markedly reduced levels of complex IV subunits. Western blots of
815 yDHODH-rescued *hdp-mNG:loxP* parasites expressing endogenous NDUFA4 (top) or Cox5B (bottom)
816 fused to mCherry. Samples were harvested at the end of the first cycle.

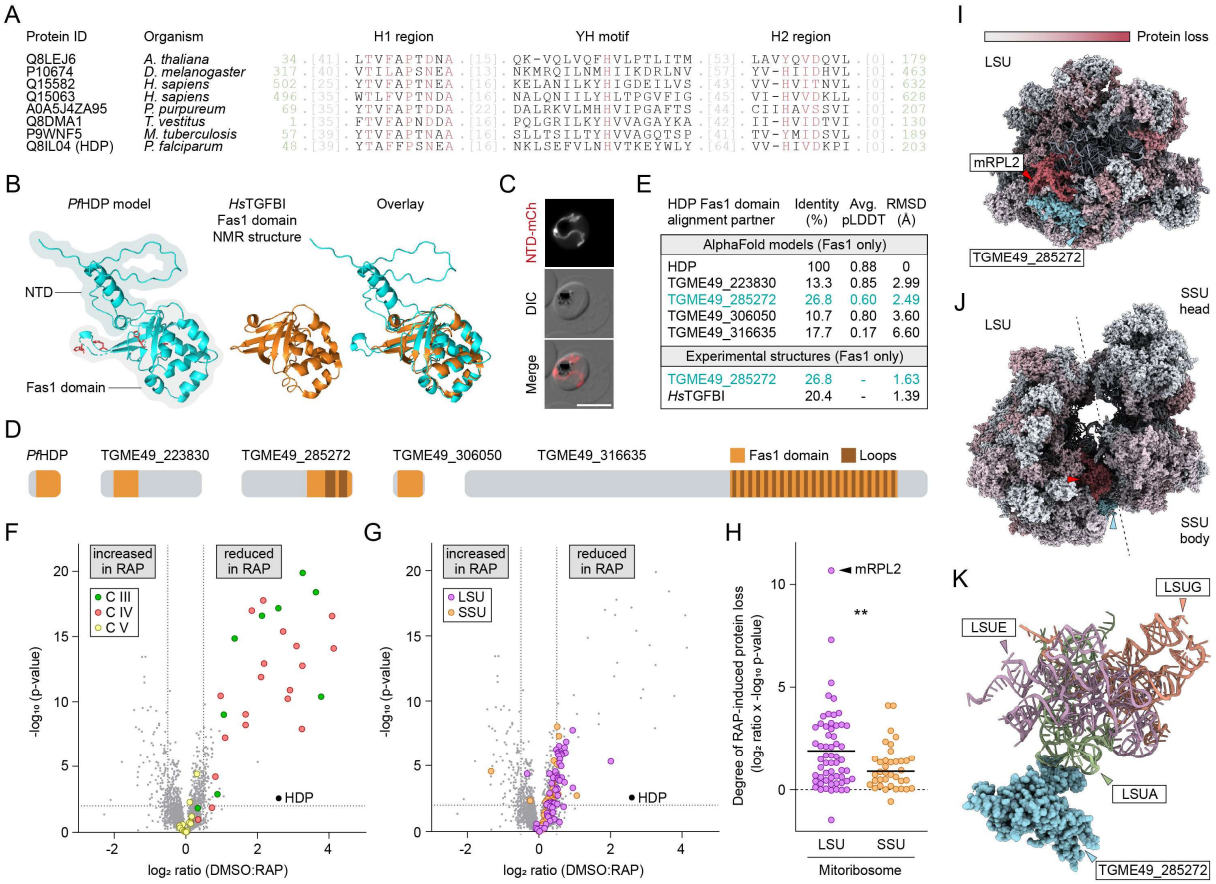

Figure 4: HDP participates in mitochondrial protein biosynthesis.

(A) Multiple sequence alignment of HDP with Fas1 domain-containing proteins from other organisms. Semi-conserved regions H1 and H2 and the YH motif are shown. Red residues indicate high conservation. Grey numbers mark omitted regions, green number denote Fas1 domain boundaries.

(B) HDP consists of a conserved Fas1 domain and a largely unstructured N-terminal domain (NTD). The AlphaFold model of HDP was aligned to the NMR structure of the human Transforming Growth Factor Beta Induced (TGFBI) Fas1 domain. Histidine residues previously implicated in β-hematin formation are highlighted in red.

(C) The NTD of HDP is sufficient for targeting mCherry to the mitochondrion. Scale bar, 5 µm.

(D) Domain organization of HDP compared with Fas1 proteins from *Toxoplasma gondii*.

(E) Sequence and structural alignments of HDP with *T. gondii* Fas1 proteins identify TGME49_285272 as the most likely HDP homolog. Sequence identity, average AlphaFold pLDDT scores, and RMSD values from structural alignments are shown.

(F-H) Whole-cell proteomics of yDHODH-rescued *hdp-mNG:loxP* parasites. (F) Subunits of complexes III (C III) and IV (C IV) are severely reduced in HDP-deficient parasites, whereas complex V (C V) remains unaffected. (G) Components of the mitoribosome's large (LSU) and small (SSU) subunits are destabilized upon loss of HDP. Note that (F) and (G) show the same dataset with different proteins highlighted. Dashed lines indicate significance and fold-change cut-offs. Benjamini-Hochberg corrected t-test; N = 4 independent biological replicates with 3 technical replicates each. (H) Loss of HDP affects the LSU more strongly than the SSU. Mean and individual values are shown for a combined score incorporating fold-change and significance. **P<0.01, unpaired t-test; N = 59 LSU, 38 SSU proteins.

838 **(I-K)** HDP-dependent reduction of *P. falciparum* mitoribosomal proteins mapped onto the *T. gondii*
839 mitoribosome structure (22). Proteins are color-coded to reflect the reduction of their respective *P.*
840 *falciparum* orthologs following HDP knockout. (I) The LSU shown from the inter-subunit side. (J) The
841 assembled mitoribosome with LSU and SSU in contact. The putative HDP ortholog TGME49_285272
842 is highlighted in cyan. (K) TGME49_285272 contacts ribosomal RNAs. Only TGME49_285272 and LSU
843 rRNAs are shown, with the rest of the *T. gondii* mitoribosome omitted for clarity.

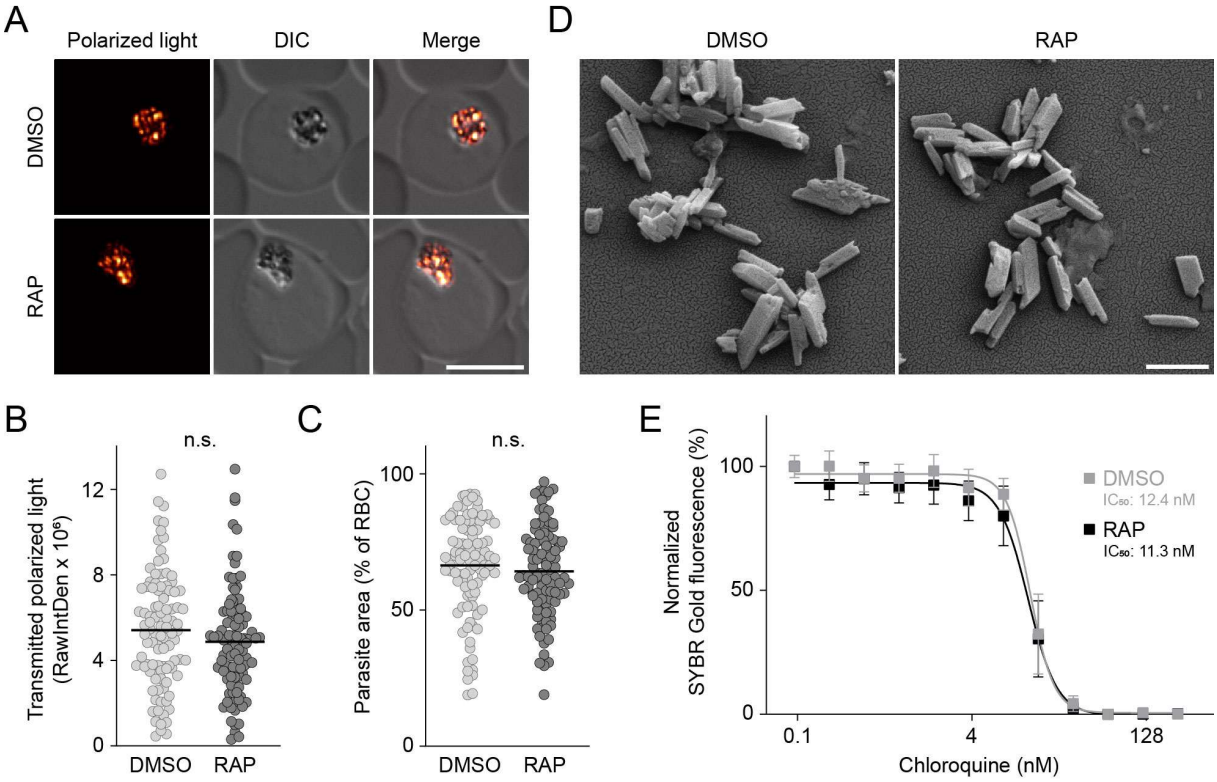

Figure 5: Loss of HDP does not affect hemozoin formation in yDHODH-rescued parasites.

To assess heme biomineralization independent of developmental arrest, metabolically rescued *hdp-mNG:loxP* + *mito-mCh* + *ydhodh* parasites were examined 36 hours post-invasion in the second cycle.

(A-C) Loss of HDP does not alter hemozoin quantity, as determined by quantitative polarization microscopy (A, B), or parasite size (C). Mean and individual values are shown. n.s., non-significant; paired t-test; N = 99 parasites from 3 independent experiments. Scale bar, 5 µm.

(D) Hemozoin morphology is unchanged in the absence of HDP, as shown by scanning electron microscopy of purified crystals. Scale bar, 500 nm.

(E) HDP-deficient parasites exhibit normal chloroquine sensitivity. Growth-response curves are shown with mean +/- SEM and IC_{50} values indicated. N = 3 biological replicates with 3 technical replicates each.

854 Supplementary material

855 for

856 Redefining the role of the *Plasmodium* heme detoxification protein: 857 From hemozoin formation to mitochondrial protein synthesis

858 Louis Sarrazin[1], Joachim Kloehn[2], Tanja Ziesmann[4], Yasmin Schmitz[1], Anna-Lena Sandtmann[1],
859 Robert Domènech Eres[1], Katharina Scholz-Höhn[3], Coralie Boulet[2], Ute Distler[4],
860 Joachim Michael Matz[1,*]

861 [1] Molecular Parasitology Group, Department of Cellular Parasitology, Bernhard Nocht Institute for Tropical Medicine, 20359
862 Hamburg, Germany

863 [2] Department of Microbiology and Molecular Medicine, Faculty of Medicine, University of Geneva, 1206 Geneva, Switzerland

864 [3] Electron Microscopy Unit, Bernhard Nocht Institute for Tropical Medicine, 20359 Hamburg, Germany

865 [4] Mass Spectrometry Core Facility, Institute for Immunology, University Medical Center Mainz, 55131 Mainz, Germany

866 * Correspondence: JMM, joachim.matz@bnitm.de

SUPPLEMENTARY METHODS

Filter-aided sample preparation

For proteome analysis, samples were prepared using a modified filter-aided sample preparation (FASP), as previously described (84, 85). Briefly, pelleted parasites were lysed in 200 µl of buffer containing 7 M urea, 2 M thiourea, 5 mM dithiothreitol (DTT), and 2% 3-[(3-cholamidopropyl)dimethylammonio]-1-propanesulfonate (CHAPS), followed by gentle vortexing and sonication at 4 °C for 15 minutes. Lysates were centrifuged at 16,200 x g for 15 minutes at 4 °C, and the supernatants were transferred into clean 1.5 mL tubes. Protein concentration was determined using the Pierce 660 nm protein assay (Thermo Fisher Scientific). 20 µg of protein were applied to Micron-30 spin filter columns (Merck) and washed three times with 8 M urea. Following reduction with DTT and alkylation with iodoacetamide (IAA), excess IAA was quenched with DTT, and the membrane was washed three times with 50 mM NH_4HCO_3. Proteins were digested overnight at 37 °C with trypsin (Promega) at a 1:50 enzyme-to-protein ratio. Peptides were recovered by centrifugation and two additional washes with 50 mM NH_4HCO_3, acidified with 1% trifluoroacetic acid, lyophilized, and reconstituted in 0.1% formic acid for LC-MS analysis.

Liquid chromatography – mass spectrometry

Proteome samples were analyzed using a nanoElute LC system coupled online to a timsTOF Pro mass spectrometer (both from Bruker). Peptides corresponding to 200 ng were loaded in direct injection mode at 600 bar onto a reversed-phase C18 column (Aurora ULTIMATE UHPLC emitter column, 25 cm x 75 µm, 1.7 µm particle size, IonOpticks) and separated at 400 nl/min at 50°C. Mobile phase A was 0.1% formic acid in water, and mobile phase B was 0.1% formic acid in acetonitrile. Separation was achieved using a linear gradient from 2% to 37% B over 39 minutes, followed by a 5-minute rinse at 95% B.

Eluting peptides were analyzed in positive-mode ESI-MS using parallel accumulation serial fragmentation enhanced data-independent acquisition (diaPASEF) (86). The dual TIMS was operated at a fixed duty cycle close to 100%, with equal accumulation and ramp times of 100 ms, each spanning a mobility range from $1/K_0 = 0.6$ to 1.6 Vs cm^{-2}. We defined 36 x 25 Th isolation windows from *m/z* 300 to 1,165, resulting in 2-3 diaPASEF scans per TIMS cycle and an overall cycle time of 1.7 seconds. Collision energy was ramped linearly as a function of mobility from 59 eV at $1/K_0 = 1.3$ Vs cm^{-2} to 20 eV at $1/K_0 = 0.85$ Vs cm^{-2}. Samples were measured in triplicate.

Raw data processing

Raw mass spectrometry data were processed using DIA-NN (version 2.2.0) (87) with default settings for library-free database search. A custom database was compiled containing the UniProtKB entries of the *P. falciparum* reference proteome and common contaminants (March 2025 release, 5,495 entries). Trypsin was specified as the protease for peptide identification and *in silico* library generation, allowing one missed cleavage. Carbamidotheylation was set as a fixed modification with no variable modifications allowed. Peptides of 7-30 amino acids were considered, with precursor *m/z* range of 300-1,800 and product ion *m/z* range of 200-1,800. For quantification, we used “QuantUMS (high precision)” mode with RT-dependent median-based cross-run normalization. Mass accuracy and scan window parameters for MS1 and MS2 were automatically optimized by DIA-NN. Peptide precursor false discovery rates were controlled below 1%.

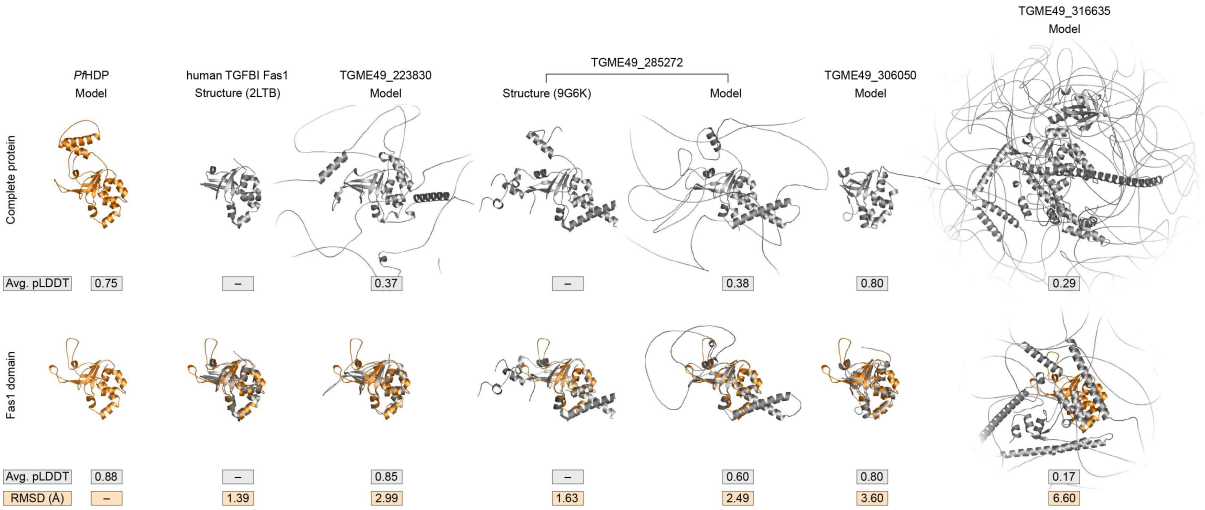

Supplementary Figure S1: Structural alignment of HDP with Fas1-domain-containing proteins from *Toxoplasma gondii*.

Shown are AlphaFold3 models of HDP and all Fas1-domain-containing proteins encoded in the *T. gondii* genome, along with the experimentally determined structures of the mitoribosomal subunit TGME49_285272 (22) and the human TGFBI Fas1 domain (50). Whole-protein structures are displayed in the top row, while the bottom row shows alignments of Fas1 domains only. Average pLDDT values for individual models and RMSD values for the alignments are indicated.

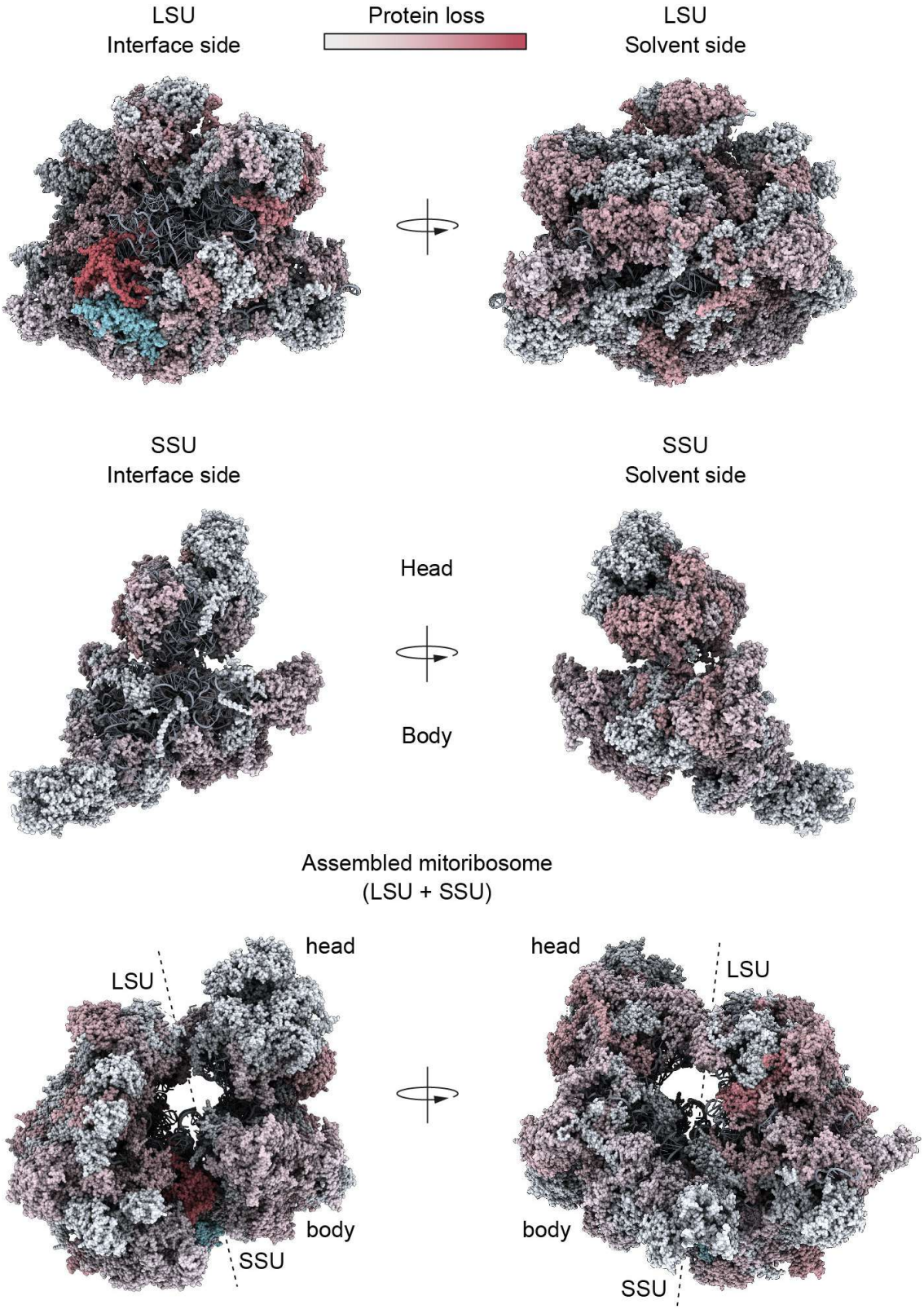

Supplementary Figure S2: HDP-dependent reduction of *P. falciparum* mitoribosomal proteins mapped onto the *T. gondii* mitoribosome structure.

Proteins are color-coded to indicate the reduction of their respective *P. falciparum* orthologs following HDP knockout. The putative HDP ortholog TGME49_285272 is highlighted in cyan. The large (LSU) and small (SSU) ribosomal subunits are shown from both the interface and solvent sides, with additional side-views of the fully assembled mitoribosome.

921 **Supplementary Table S1: Oligonucleotides and synthetic repair template used in this study.**

Template	Oligo[1]	Oligo sequence[2]	Amplicon size (bp)[3]
Diagnostic PCRs			
HDP locus	PCR 1, F	GGATTAGCCGACAAAAATTAAGG	WT 889 / Mutant –
HDP locus	PCR 1, R	ATTCATGTATTAACGAGCTGCC	WT 889 / Mutant –
HDP locus	PCR 2, F	TGAATTATCTCTCGATGGCCC	WT 2,034 / Mutant –
HDP locus	PCR 2, R	TTATTTAAGAGAGTTTGATTTATTATCTGG	WT 2,034 / Mutant –
HDP locus	PCR 3, F	GGATTAGCCGACAAAAATTAAGG	WT – / Mutant 807
HDP locus	PCR 3, R	ATAACTTCGTATAATGTATGCTATACGAAG	WT – / Mutant 807
HDP locus	PCR 4, F	AACTTCGTATAGCATACATTATACGAAG	WT – / Mutant 1,593
HDP locus	PCR 4, R	TTATTTAAGAGAGTTTGATTTATTATCTGG	WT – / Mutant 1,593
HDP locus	PCR 5, F	AATGTGTAGAATGTATTTTTCATCAG	DMSO 1,726 / RAP 507
HDP locus	PCR 5, R	TAAAACTACCTTAATGAAAAACAACATATG	DMSO 1,726 / RAP 507
Cloning PCRs			
mCh	F	aaaaaaacgcgtgctagaggtgctgctgctggtgctggaggtgcaggtagacgtacgATGGTGAGCAAGGGCG	777
mCh	R	aaaatagtcgacCTTGTACAGCTCGTCCATG	777
mNG	F	aaatttgatatcggagcaggtgcaggtATGGTAAGTAAGGGAGAAGAAGAC	747
mNG	R	tttttagatatcCTTATACAACTCATCCATTCCCATTAC	747
Cox5B	CT, F	aattatgcggccgctaaCCGAAGCAACTAAACTTTTGTGGA	1,063
Cox5B	CT, R	atatttacgcgtTGTGTTTGGTTTTTGGTTTCCCCATTTTCC	1,063
NDUFA4	CT, F	attaaaagcggccgctaaCTCATATTTCAGAACGCACAACAT	567
NDUFA4	CT, R	atatttacgcgtAACTCGCATGTTTTCTGGTTTTTG	567
HDP	F	aaactactcgagATGAAAAATAGATTTTATTATAATTTGATAATTAAAAGATTATATACAC	654_{cDNA}
HDP	R	aaattcggtacctcctgctcctgctccAAAAATGATGGGCTTATCTACTATATGC	654_{cDNA}
HDP	NTD, F	aaactactcgagATGAAAAATAGATTTTATTATAATTTGATAATTAAAAGATTATATACAC	204
HDP	NTD, R	ttttttggtacctcctgctcctgctccTATTAAATTAATAATTGTCCTTTTTACAG	204
Guide plasmid construction[4]			
–	F	attgTCATCCTACAGGTAACAACA	–
–	R	aaacTGTTGTTACCTGTAGGATGA	–

Repair template sequence[5]

AATGATTGTCATTTATTTTCATAATAATTCTTTCTCAAATGTAAGAAAAGAAAATGATAACTTTTGTTAAACATAAAACATTT
CTTTTTTTTTCTTTTTTTTTTGGTCTAAATAATATATATTGTATTATATTGTATTACATTATATATCTGTATAAATGTGTAGAAT
GTATTTTTCATCAGTATGAAAAATAGATTTTATTATAATTTGATAATTAAAAGATTATATACACGAAGTGGCGGTTTAAGAAA
ACCTCAAAAGGTAACCAACGACCCAGAAAGTATAAATAGAAAAGTATATTGGTGTTTTGAACATAAGCCTGTAAAAAGGA
CAATTATTAATTTAATATATTCACATAACGAACTCAAGATATTTTCTAATCTGTTAAATCATCCTACAGGTAAATAAAAAAAA
TAATATACAATAACTTCGTATAGCATACATTATACGAAGTTATTATATATGTATATATATATATATTTATATATTTTATATTCT
TTTAGTTGGCTCATCATTGATACACGAGCTTTCATTAGACGGTCCTTACACTGCATTTTTCCCAAGTAACGAAGCCATGCA
GTTAATAAACATAGAGTCATTCAACAAGTTATACAATGATGAAAACAAGTTGTCAGAGTTCGTTCTTAATCACGTGACCAA
GGAATACTGGTTGTACCGTGATTTATACGGATCTTCTTATCAGCCTTGGCTTATGTACAATGAAAAAAGGGAGGCTCCAG
AGAAATTGAGGAACTTACTTAATAACGACTTGATTGTAAAAATAGAAGGTGAATTCAAGCATTGTAACCACTCTATATATTT
GAATGGTAGTAAGATTATTAGACCTAACATGAAGTGCCACAATGGAGTGGTACACATTGTTGATAAGCCTATAATATTTGT
TATCGGAGCAGGTGCAGGTATGGTAAGTAAGGGAGAAGAAGACAACATGGCATCATTGCCAGCCACCCACGAGTTGCA
TATTTTCGGTTCTATTAACGGAGTGGACTTTGATATGGTTGGTCAGGGTACAGGAAATCCTAATGATGGTTATGAGGAGC
TTAATTTGAAATCTACTAAAGGTGACTTGCAGTTTTCACCTTGGATACTTGTTCCACATATAGGTTACGGTTTTCACCAGTA
CCTTCCATATCCAGATGGAATGTCTCCATTCCAGGCTGCTATGGTGGATGGAAGTGGTTATCAAGTACATAGGACCATGC
AGTTTGAGGACGGTGCATCTTTAACCGTTAACTATAGATATACCTATGAAGGATCTCACATTAAAGGTGAAGCCCAAGTG
AAAGGTACCGGATTTCCTGCTGACGGTCCAGTGATGACTAACAGTTTAACTGCCGCAGACTGGTGCCGTTCTAAAAAGA
CATATCCAAACGATAAGACTATAATTTCTACCTTTAAATGGTCATACACAACAGGAAATGGAAAACGTTATAGATCAACTG
CAAGGACTACTTATACATTCGCTAAACCAATGGCCGCCAATTATCTTAAAAATCAACCTATGTATGTTTTCCGTAAAACTG
AATTAAAGCACTCAAAGACAGAACTTAATTTTAAGGAATGGCAAAAAGCATTTACTGACGTAATGGGAATGGATGAGTTGT
ATAAGGATAACTAAAATATAACTTCGTATAGCATACATTATACGAAGTTATAAAACAACACAGATAAATTAACACACACACA
CATATATATATATATATATATATTAATTTATTTGTTATATATTTATGATTTATTTTAAAAATATTATTTTTTTTATTTTTATGG
GAAAAATGAAGGATATTCCTTTTTCATTTTAAAAATATGTTTTTACTTGAAAAATATTACATATGTTGTTTTTCATTAAGGTA
GTTTTAAAACATCAACAATTTATTACATACATATATATATTATAAAAGTGTAATATAATTGTTCTTTTAAAATAATAAATAAAT
TATAAAAAAAATATAAAAATATAAAATATAAGGATAACCTAGTACATATTATATGAAACAAAAAAAAAAAAAAAAAAAAAAA
ATGGTATATTAAAATTTTTTTTTTTACAAAAAA

[1] PCRs 1-5 indicate the relative primer positions as shown in Figure 1A. CT: carboxy-terminus; NTD: amino-terminal domain; F: forward primer; R: reverse primer.

[2] Annealing bases are shown in upper case, overhangs in lower case.

[3] Expected PCR fragments for wild-type (WT) and mutant parasites.

[4] Complementary oligonucleotides were annealed, phosphorylated and cloned into the pDC2-Cas9-U6-hDHFRyFCU plasmid using BbsI

[5] Grey, homology regions; red, start and stop codons; light blue, artificial intron; dark blue, *LoxP* sites; orange, recodonized HDP sequence; purple, linker; green, mNG.

Supplementary Table S2: Quantitative proteomic analysis of respiratory chain complexes and mitoribosomal subunits.

Protein complex	Protein name	Gene accession code	Log_2 ratio (DMSO vs RAP)	t-test p-value	p-value (BH-adjusted)	BH-adjusted incl. p-value cutoff	Significance (incl. all cutoffs and minimal replicate number)	$-log_{10}$ (BH-adjusted incl. p-value cutoff)	Combined score (log_2 ratio * $-log_{10}$ t-test)
C III	C3AP2	PF3D7_1326000	3.632510144	3.99413E-19	3.38382E-16	3.99413E-19	sig. reduced in RAP	18.39857833	66.83302243
C III	C3AP1	PF3D7_0722700	3.264150877	1.32216E-20	1.40017E-17	1.32216E-20	sig. reduced in RAP	19.87871461	64.88712374
C III	QCR7	PF3D7_1012300	2.585827027	6.72406E-18	4.06902E-15	6.72406E-18	sig. reduced in RAP	17.17236858	44.40477479
C III	C3AP3	PF3D7_0817800	2.126512933	2.54409E-17	1.13244E-14	2.54409E-17	sig. reduced in RAP	16.59446689	35.28834846
C III	QCR9	PF3D7_0622600	1.362051197	1.43129E-15	5.05246E-13	1.43129E-15	sig. reduced in RAP	14.84427224	20.21865878
C III	Rieske	PF3D7_1439400	1.060104771	9.70399E-10	1.17446E-07	9.70399E-10	sig. reduced in RAP	9.013049489	9.554776766
C III	QCR6	PF3D7_1426900	0.885486788	0.00131469	0.015010854	0.00131469	sig. reduced in RAP	2.881176631	2.551243841
C III	Cytochrome c1	PF3D7_1462700	0.334799181	0.014941159	0.090157765	n.s.	n.s.	0	0
C III	QCR2	PF3D7_0523100	-0.043606738	0.75002376	0.969810942	n.s.	n.s.	0	0
C III	QCR1	PF3D7_0933600	-0.046416667	0.762289696	0.970700397	n.s.	n.s.	0	0
C III	QCR8	PF3D7_0306000	0.025249205	0.910427375	0.993705323	n.s.	n.s.	0	0
C IV	C4AP5	PF3D7_0809250	n.d. in RAP	n.d. in RAP	n.d. in RAP	n.d. in RAP	sig. reduced in RAP	n.d. in RAP	n.d. in RAP
C IV	COX1	PF3D7_MIT02100	n.d. in RAP	n.d. in RAP	n.d. in RAP	n.d. in RAP	sig. reduced in RAP	n.d. in RAP	n.d. in RAP
C IV	C4AP1	PF3D7_1125600	4.087945236	2.67338E-17	1.13244E-14	2.67338E-17	sig. reduced in RAP	16.57293898	67.74926693
C IV	APICOX16	PF3D7_1345300	4.131859854	8.06036E-15	2.43883E-12	8.06036E-15	sig. reduced in RAP	14.09364582	58.23296935
C IV	COX6A	PF3D7_1465000	3.090695606	5.27902E-15	1.72015E-12	5.27902E-15	sig. reduced in RAP	14.27744645	44.12724101
C IV	COX6B	PF3D7_0928000	2.719153623	4.06051E-16	1.56367E-13	4.06051E-16	sig. reduced in RAP	15.39141895	41.85163259
C IV	APICOX19	PF3D7_1402200	3.258388797	1.74863E-13	4.11512E-11	1.74863E-13	sig. reduced in RAP	12.75730101	41.56824671
C IV	Cytochrome b	PF3D7_MIT02300	3.781634365	4.12437E-11	6.98833E-09	4.12437E-11	sig. reduced in RAP	10.38464267	39.27092157
C IV	COX4	PF3D7_0708700	2.162593918	1.73127E-18	1.22228E-15	1.73127E-18	sig. reduced in RAP	17.76163509	38.41120403
C IV	APICOX24	PF3D7_1362000	2.911556571	1.29621E-11	2.49579E-09	1.29621E-11	sig. reduced in RAP	10.88732518	31.69906316
C IV	COX6C	PF3D7_0306500	1.844347708	1.03394E-17	5.47471E-15	1.03394E-17	sig. reduced in RAP	16.98550466	31.32717659
C IV	APICOX14	PF3D7_1339400	2.846741353	5.94923E-11	9.69267E-09	5.94923E-11	sig. reduced in RAP	10.22553898	29.10946466
C IV	COX2A	PF3D7_1361700	2.186894074	1.16655E-13	2.90677E-11	1.16655E-13	sig. reduced in RAP	12.93309578	28.28331052
C IV	NDUFA4	PF3D7_1439600	3.242599895	1.22522E-08	1.23572E-06	1.22522E-08	sig. reduced in RAP	7.91178611	25.65475681
C IV	APICOX18	PF3D7_0523300	2.101469172	1.2673E-12	2.68415E-10	1.2673E-12	sig. reduced in RAP	11.89711982	25.00143054
C IV	APICOX30	PF3D7_0915700	1.669862786	9.33969E-10	1.16362E-07	9.33969E-10	sig. reduced in RAP	9.02966763	15.07830595
C IV	COX5B	PF3D7_0927800	1.670592669	6.06679E-09	6.94565E-07	6.06679E-09	sig. reduced in RAP	8.217041085	13.7273286
C IV	C4AP2	PF3D7_1025800	0.97312271	3.59438E-11	6.34408E-09	3.59438E-11	sig. reduced in RAP	10.44437584	10.16365932
C IV	APICOX13	PF3D7_1022900	1.097229868	5.83429E-08	4.49346E-06	5.83429E-08	sig. reduced in RAP	7.23401204	7.937374075
C IV	COX2B	PF3D7_1430900	0.827122789	6.23883E-05	0.001362251	6.23883E-05	sig. reduced in RAP	4.20489718	3.477966281
C IV	C4AP3	PF3D7_1003100	0.73024167	0.013899812	0.085086132	n.s.	n.s.	0	0
C IV	C4AP4	PF3D7_0608400	0.138199858	0.170828106	0.465056462	n.s.	n.s.	0	0
C V	ATP i/j	PF3D7_1360000	0.310547599	3.88564E-05	0.000956951	3.88564E-05	n.s.	4.410537974	1.369681977
C V	ATP gamma	PF3D7_1311300	0.112933346	0.00522953	0.042875953	0.00522953	n.s.	2.281537372	0.25766165
C V	ATPTG2	PF3D7_0611300	0.164135521	0.062758931	0.24351812	n.s.	n.s.	0	0
C V	ATPTG12	PF3D7_0620100	0.119533751	0.160246266	0.444533846	n.s.	n.s.	0	0
C V	ICAP2	PF3D7_1125100	0.093213096	0.181815676	0.486526345	n.s.	n.s.	0	0
C V	OCSP	PF3D7_1310000	0.137990629	0.213785946	0.534906833	n.s.	n.s.	0	0
C V	ATPTG9	PF3D7_1417900	-0.082310508	0.255475827	0.593828059	n.s.	n.s.	0	0
C V	ATPTG4	PF3D7_0905000	-0.177700808	0.316560823	0.672830731	n.s.	n.s.	0	0
C V	ATP beta	PF3D7_1235700	-0.16457811	0.466746038	0.831148078	n.s.	n.s.	0	0

C V	ATPTG6	PF3D7_1142800	-0.091310965	0.663478209	0.950641315	n.s.	n.s.	0	0
C V	ATPTG13	PF3D7_1303000	0.034075498	0.748642251	0.968615936	n.s.	n.s.	0	0
C V	ATPTG10	PF3D7_1024300	-0.041748422	0.832359746	0.981146185	n.s.	n.s.	0	0
C V	ATP d	PF3D7_0311800	-0.021765481	0.878761534	0.987055235	n.s.	n.s.	0	0
C V	ATP alpha	PF3D7_0217100	0.012049497	0.927411088	0.993984834	n.s.	n.s.	0	0
LSU	uL2m	PF3D7_1132700	2.006536504	4.79229E-06	0.000189721	4.79229E-06	sig. reduced in RAP	5.319457149	10.67368495
LSU	uL6m	PF3D7_1224800	0.94225431	1.76157E-08	1.65823E-06	1.76157E-08	sig. reduced in RAP	7.754099422	7.306333599
LSU	mL163	PF3D7_1233800	0.760308738	1.39129E-07	9.82248E-06	1.39129E-07	sig. reduced in RAP	6.856583733	5.213120528
LSU	mL154	PF3D7_1004900	0.714927612	3.78512E-07	2.32374E-05	3.78512E-07	sig. reduced in RAP	6.421919835	4.591207811
LSU	mL179	PF3D7_0715700	0.74034651	9.63711E-07	4.80268E-05	9.63711E-07	sig. reduced in RAP	6.016053188	4.453963983
LSU	uL29m	PF3D7_0315500	0.632753826	1.21268E-06	5.83739E-05	1.21268E-06	sig. reduced in RAP	5.916254687	3.743532791
LSU	bL21m	PF3D7_1422100	0.565947511	2.97204E-07	1.90751E-05	2.97204E-07	sig. reduced in RAP	6.52694548	3.693908552
LSU	uL4m	PF3D7_0822000	0.627906958	1.50178E-06	6.91473E-05	1.50178E-06	sig. reduced in RAP	5.823393167	3.656549091
LSU	uL1m	PF3D7_0710900	0.594873579	9.32216E-07	4.74461E-05	9.32216E-07	sig. reduced in RAP	6.030483286	3.587375173
LSU	mL155	PF3D7_1114400	0.538048531	8.82E-07	4.61254E-05	8.82E-07	sig. reduced in RAP	6.054531251	3.257631646
LSU	mL158	PF3D7_0921300	0.588036485	3.25049E-06	0.000140501	3.25049E-06	sig. reduced in RAP	5.488051525	3.22717453
LSU	uL24m-b	PF3D7_1223900	0.54956594	1.64303E-06	7.48375E-05	1.64303E-06	sig. reduced in RAP	5.784353622	3.178883734
LSU	bL9m	PF3D7_1363300	0.528317644	1.1491E-06	5.59491E-05	1.1491E-06	sig. reduced in RAP	5.93964372	3.138018578
LSU	mL172	PF3D7_1465400	0.944680872	0.000489616	0.007153845	0.000489616	sig. reduced in RAP	3.310144564	3.127030253
LSU	uL13m	PF3D7_0214200	0.622652635	1.09243E-05	0.000355245	1.09243E-05	sig. reduced in RAP	4.961607585	3.089358039
LSU	uL3m	PF3D7_1245400	0.486588216	5.4486E-07	3.11895E-05	5.4486E-07	n.s.	6.263715412	3.047850105
LSU	bL35m	PF3D7_1025700	0.574586904	6.93484E-06	0.000251077	6.93484E-06	sig. reduced in RAP	5.158963764	2.964273016
LSU	mL164	PF3D7_0313200	0.716367977	0.000192003	0.003374783	0.000192003	sig. reduced in RAP	3.716693092	2.662519911
LSU	mL64	PF3D7_0720600	0.636652717	8.32175E-05	0.001682837	8.32175E-05	sig. reduced in RAP	4.079785171	2.597406314
LSU	uL15m	PF3D7_1429700	0.522433505	1.23981E-05	0.000389024	1.23981E-05	sig. reduced in RAP	4.906645347	2.563395925
LSU	mL43	PF3D7_1010000	0.544563284	7.50194E-05	0.00157318	7.50194E-05	sig. reduced in RAP	4.124826303	2.246228959
LSU	mL159	PF3D7_1135500	0.54285477	0.00012202	0.002360167	0.00012202	sig. reduced in RAP	3.91356914	2.124499677
LSU	mL150	PF3D7_0317900	0.499969283	5.95623E-05	0.001312972	5.95623E-05	n.s.	4.2250284	2.11238442
LSU	mL174	PF3D7_1134400	0.523004726	9.54542E-05	0.001907284	9.54542E-05	sig. reduced in RAP	4.020204824	2.102586121
LSU	uL11m	PF3D7_1110600	0.460172597	2.91366E-05	0.000757194	2.91366E-05	n.s.	4.535561434	2.087141083
LSU	mRPL33	PF3D7_0210400	0.51896684	0.000626967	0.008415137	0.000626967	sig. reduced in RAP	3.202755322	1.662123809
LSU	mL41	PF3D7_0604200	0.498525144	0.00049472	0.007190756	0.00049472	n.s.	3.305640575	1.647944943
LSU	mL153	PF3D7_1009300	0.395019316	8.34267E-05	0.001682837	8.34267E-05	n.s.	4.078694693	1.611163188
LSU	mL40	PF3D7_1036600	0.463485515	0.000692174	0.00919137	0.000692174	n.s.	3.159785022	1.464514588
LSU	bL17m	PF3D7_1431000	0.523189089	0.001838624	0.019471026	0.001838624	sig. reduced in RAP	2.735507126	1.431187481
LSU	bL28m	PF3D7_1456600	0.354658661	0.000227036	0.003831566	0.000227036	n.s.	3.643905909	1.29234279
LSU	mL160	PF3D7_1029800	0.292985527	4.03151E-05	0.000981464	4.03151E-05	n.s.	4.394532296	1.28753436
LSU	mL177	PF3D7_0312000	0.511159775	0.008158972	0.058184185	0.008158972	sig. reduced in RAP	2.088364552	1.067487954
LSU	mL173	PF3D7_0111200	0.435240873	0.007216266	0.054102838	0.007216266	n.s.	2.141687453	0.932149916
LSU	uL23m	PF3D7_1239100	0.417185899	0.006676678	0.051321423	0.006676678	n.s.	2.17543957	0.907562712
LSU	bL32m	PF3D7_0213300	0.299605454	0.00126222	0.014529254	0.00126222	n.s.	2.898864825	0.868515712
LSU	mL54	PF3D7_1123700	0.35913588	0.006080246	0.048052094	0.006080246	n.s.	2.216078846	0.795873426
LSU	mL49	PF3D7_1144100	0.281827939	0.006687778	0.051321423	0.006687778	n.s.	2.174718182	0.612896343
LSU	mL152	PF3D7_1448800	0.24957432	0.007935766	0.057365022	0.007935766	n.s.	2.100411168	0.524208689
LSU	mL162	PF3D7_0502700	0.213492547	0.009194293	0.063743083	0.009194293	n.s.	2.036481676	0.434773659
LSU	mL149	PF3D7_1409700	0.164818751	0.007471342	0.055329729	0.007471342	n.s.	2.126601376	0.350503784
LSU	mL156	PF3D7_1033000	0.309931479	0.013220127	0.082474898	n.s.	n.s.	0	0
LSU	bL19m	PF3D7_0610000	0.687258893	0.013518817	0.08356858	n.s.	n.s.	0	0
LSU	mL180	PF3D7_1204700	0.378876184	0.015787398	0.094190728	n.s.	n.s.	0	0

LSU	bL25m	PF3D7_0406800	0.391123023	0.036479316	0.169809211	n.s.	n.s.	0	0
LSU	uL24m	PF3D7_0605000	0.227487502	0.039889152	0.181298763	n.s.	n.s.	0	0
LSU	mL46	PF3D7_0626900	0.236354517	0.062587279	0.24350763	n.s.	n.s.	0	0
LSU	mL170	PF3D7_1202400	0.260209624	0.075559926	0.274504157	n.s.	n.s.	0	0
LSU	uL14m	PF3D7_0519100	0.427224519	0.117586746	0.364464956	n.s.	n.s.	0	0
LSU	mL171	PF3D7_0934400	0.311975835	0.160094871	0.444533846	n.s.	n.s.	0	0
LSU	mL175	PF3D7_0512100	0.574688969	0.195529875	0.508449694	n.s.	n.s.	0	0
LSU	mL151	PF3D7_0105200	-0.064490541	0.263373913	0.605674211	n.s.	n.s.	0	0
LSU	bL12m	PF3D7_0212200	0.197397053	0.277643021	0.625250311	n.s.	n.s.	0	0
LSU	bL27m	PF3D7_0316100	0.048781324	0.533259837	0.88134556	n.s.	n.s.	0	0
LSU	mL182	PF3D7_1024200	-0.083861987	0.559190847	0.901390176	n.s.	n.s.	0	0
LSU	mL176	PF3D7_0821900	0.156529395	0.561308974	0.90372665	n.s.	n.s.	0	0
LSU	mL167	PF3D7_1115500	-0.040010028	0.692916132	0.952550654	n.s.	n.s.	0	0
LSU	mL166	PF3D7_0611200	0.019416526	0.96808582	0.997431654	n.s.	n.s.	0	0
LSU	uL22m	PF3D7_1010800	13.79555346	9999	1	n.s.	n.s.	0	0
LSU	mL169	PF3D7_0705600	-0.331815343	4.17555E-05	0.001010722	4.17555E-05	n.s.	4.379286302	-1.453114387
SSU	uS5m	PF3D7_0713600	0.51140067	9.19856E-09	9.74128E-07	9.19856E-09	sig. reduced in RAP	8.036280149	4.109759053
SSU	mS33	PF3D7_1242500	0.561772041	5.01414E-08	4.00753E-06	5.01414E-08	sig. reduced in RAP	7.299803273	4.100825384
SSU	uS14m	PF3D7_1447300	1.058639607	0.00191506	0.019857962	0.00191506	sig. reduced in RAP	2.717817702	2.877189464
SSU	mS143	PF3D7_1314300	0.504693803	7.83548E-06	0.000268184	7.83548E-06	sig. reduced in RAP	5.105934374	2.576933436
SSU	mS149	PF3D7_1366200	0.608045014	0.000141582	0.00264203	0.000141582	sig. reduced in RAP	3.848992341	2.3403606
SSU	mS160	PF3D7_1319500	0.494909392	2.15776E-05	0.000609351	2.15776E-05	n.s.	4.665997151	2.309245813
SSU	mS152	PF3D7_1228000	0.413190591	4.33239E-06	0.000178175	4.33239E-06	n.s.	5.363272076	2.216053559
SSU	bS21m	PF3D7_1452900	0.452322699	2.75345E-05	0.00073356	2.75345E-05	n.s.	4.560123008	2.062647148
SSU	mS137	PF3D7_1318600	0.457748539	7.82348E-05	0.001601817	7.82348E-05	n.s.	4.106599918	1.879790113
SSU	uS8m	PF3D7_0718400	0.542087251	0.001570804	0.01706294	0.001570804	sig. reduced in RAP	2.803878103	1.519946572
SSU	mS140	PF3D7_1436700	0.344501044	4.71618E-05	0.001122346	4.71618E-05	n.s.	4.326409229	1.490452497
SSU	mS147	PF3D7_0624100	0.382168749	0.00022494	0.003826697	0.00022494	n.s.	3.647932566	1.394125826
SSU	mS23	PF3D7_0728300	0.382036734	0.000235324	0.003955693	0.000235324	n.s.	3.628332876	1.38615644
SSU	mS145	PF3D7_0408400	0.394790481	0.000329826	0.005241362	0.000329826	n.s.	3.481715568	1.374548164
SSU	mS146	PF3D7_1024700	0.413001655	0.000486805	0.007153845	0.000486805	n.s.	3.312645216	1.368127957
SSU	bS18m	PF3D7_1211500	0.402549658	0.000519866	0.007365062	0.000519866	n.s.	3.284108385	1.322016706
SSU	mS156	PF3D7_0406600	0.457913971	0.001344869	0.015173691	0.001344869	n.s.	2.871320055	1.31481757
SSU	uS9m	PF3D7_1137100	0.374942171	0.001105693	0.013193569	0.001105693	n.s.	2.956365316	1.10846603
SSU	mS35	PF3D7_1312300	0.393702708	0.004446111	0.038279928	0.004446111	n.s.	2.352019738	0.925996539
SSU	mS150	PF3D7_1305200	0.341520481	0.003207556	0.02986199	0.003207556	n.s.	2.493825809	0.851692591
SSU	mS155	PF3D7_1336100	0.367146718	0.005998076	0.04784906	0.005998076	n.s.	2.221988023	0.815795611
SSU	mS151	PF3D7_0305400	0.27997383	0.002751741	0.026612731	0.002751741	n.s.	2.560392389	0.716842863
SSU	uS15m	PF3D7_1310900	0.31064038	0.00496035	0.041392199	0.00496035	n.s.	2.304487687	0.71586693
SSU	mS41	PF3D7_1309800	0.248286561	0.003525518	0.032116335	0.003525518	n.s.	2.452777025	0.608991572
SSU	mS34	PF3D7_1460200	0.239377553	0.009054993	0.0629835	0.009054993	n.s.	2.043111865	0.489075119
SSU	mS45	PF3D7_0105500	0.221187901	0.00980928	0.06691161	0.00980928	n.s.	2.008362874	0.444225569
SSU	mS26	PF3D7_1012100	0.185016288	0.005526151	0.044930472	0.005526151	n.s.	2.257577249	0.417688563
SSU	mS29	PF3D7_1445300	0.218595208	0.010598933	0.070704066	n.s.	n.s.	0	0
SSU	mS154	PF3D7_0318200	-0.200692521	0.028422814	0.142315652	n.s.	n.s.	0	0
SSU	mS47	PF3D7_1017200	0.159093755	0.033540747	0.160540798	n.s.	n.s.	0	0
SSU	uS11m	PF3D7_1454600	0.340795351	0.039403466	0.179476433	n.s.	n.s.	0	0
SSU	bS16m	PF3D7_0531200	0.144132336	0.056153941	0.225467388	n.s.	n.s.	0	0
SSU	mS144	PF3D7_0812000	0.192459795	0.141985484	0.410880532	n.s.	n.s.	0	0

SSU	uS10m	PF3D7_0521200	0.107117371	0.194536214	0.507111016	n.s.	n.s.	0	0
SSU	uS2m	PF3D7_0934200	0.102422826	0.288291866	0.6386718	n.s.	n.s.	0	0
SSU	mS139	PF3D7_1437600	0.078592311	0.365848424	0.731006568	n.s.	n.s.	0	0
SSU	mS159	PF3D7_0622400	0.085465953	0.623135257	0.935801675	n.s.	n.s.	0	0
SSU	mS148	PF3D7_0605200	0.121440196	0.662188444	0.950641315	n.s.	n.s.	0	0
SSU	mS142	PF3D7_1034800	0.003307647	0.96613701	0.997182301	n.s.	n.s.	0	0
SSU	mS37	PF3D7_0105100	-0.243924411	0.004561355	0.039192494	0.004561355	sig. reduced in RAP	2.34090613	-0.571004149

931 **Supplementary Table S3: Transgenic parasite strains used in this study.**

Mutant	Parental strain[1]	Description[2]
B11	3D7	Constitutive expression of DiCre recombinase
hdp-mNG:loxP	B11	Conditional deletion of mNG-tagged HDP by DiCre
hdp-mNG:loxP + mito-mCh + ydhodh	*hdp-mNG:loxP*	Episomal expression of mitochondrial marker in HDP-mNG DiCre line
hdp-mNG:loxP + apico-mCh + bsd	*hdp-mNG:loxP*	Episomal expression of apicoplast marker in HDP-mNG DiCre line
hdp-mCh + ydhodh	3D7	Episomal expression of mCh-tagged HDP
ntd-mCh + ydhodh	3D7	Episomal expression of mCh-tagged HDP N-terminal domain
hdp-mNG:loxP + ydhodh	*hdp-mNG:loxP*	Phenotypic rescue of HDP-mNG DiCre line by yDHODH
hdp-mNG:loxP + cox5b-mCh	*hdp-mNG:loxP*	Endogenous mCh-tagging of Cox5B in HDP-mNG DiCre line
hdp-mNG:loxP + ndufa4-mCh	*hdp-mNG:loxP*	Endogenous mCh-tagging of NDUFA4 in HDP-mNG DiCre line
hdp-mNG:loxP + cox5b-mCh + ydhodh	*hdp-mNG:loxP + cox5b-mCh*	Phenotypic rescue of HDP-mNG DiCre line expressing mCh-tagged Cox5B by yDHODH
hdp-mNG:loxP + ndufa4-mCh + ydhodh	*hdp-mNG:loxP + ndufa4-mCh*	Phenotypic rescue of HDP-mNG DiCre line expressing mCh-tagged Cox5B by yDHODH

932 [1] Recipient strains used as genetic background for parasite transfection.
933 [2] DiCre, dimerizable Cre recombinase; mCh, mCherry; mNG, mNeonGreen; yDHODH, yeast dihydroorotate dehydrogenase.